

TEL AVIV UNIVERSITY

The Iby and Aladar Fleischman Faculty of Engineering

The Zandman-Slaner School of Graduate Studies

**CELLULAR INTERNALIZATION OF
SINGLE-WALLED CARBON NANOTUBES
ENHANCED BY A TRANSFECTION REAGENT
ASSESSED BY NEAR-INFRARED FLUORESCENCE
IMAGING**

A thesis submitted toward the degree of
Master of Science in Biomedical Engineering

by

Naamah Levin

December 2023

TEL AVIV UNIVERSITY

The Iby and Aladar Fleischman Faculty of Engineering

The Zandman-Slaner School of Graduate Studies

**CELLULAR INTERNALIZATION OF
SINGLE-WALLED CARBON NANOTUBES
ENHANCED BY A TRANSFECTION REAGENT
ASSESSED BY NEAR-INFRARED FLUORESCENCE
IMAGING**

A thesis submitted toward the degree of
Master of Science in Biomedical Engineering

by

Naamah Levin

This research was carried out in The Department of Biomedical Engineering

Under the supervision of Prof. Gili Bisker

December 2023

Acknowledgments

First and foremost, I would like to thank my supervisor, Prof. Gili Bisker, for her ongoing guidance, encouragement, and support, for pushing me professionally and believing in me and in my research. For being an inspiration for professionalism and high work ethics, all with a smile and patience.

I would like to thank Dr. Adi Hendler-Neumark for the initial training, support, and involvement, Dr. Dotan Kamber for endless help, support, and patience with using the imaging microscope, Dr. Verena Wulf for her technical support and help when needed, Eddie Sharaga for being a supportive partner in the process and everyone else in the Bisker Lab group who created a friendly and pleasant environment to work in.

I would also like to thank the Faculty of Engineering at Tel Aviv University for the Fellowship for excellent graduate students, and the Einav family for the financial support towards this research in honor of the late Professor Shmuel Einav, founder of the Biomedical Engineering Department at Tel Aviv University.

Finally, I would like to express my deepest gratitude to Ezra and my family, for believing in me, for their continuous support, and for picking up the slack when needed, which enabled this research to thrive.

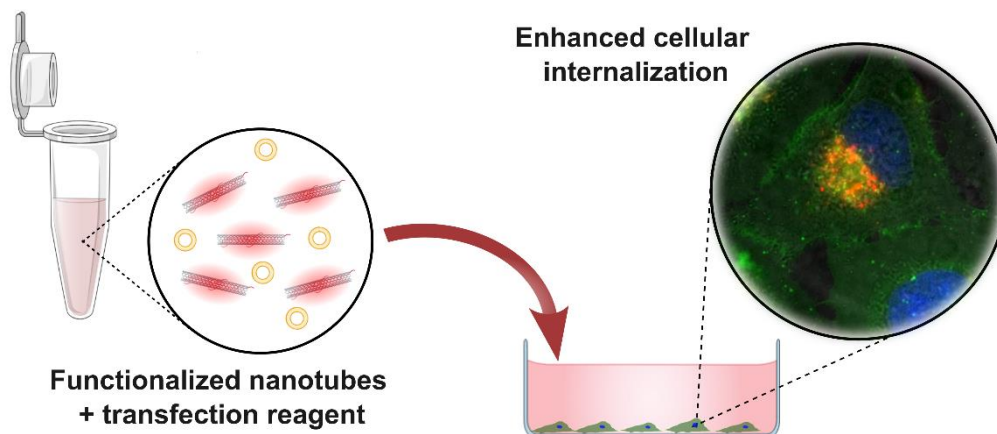
Abstract

Nanoparticles, with dimensions comparable to those of cell organelles, have emerged as a promising technology for biomedical applications on the cellular level. Amongst them, are biosensing, imaging, and drug-delivery vehicles. Therefore, the cellular uptake of the nanoparticles, which involves overcoming the cell plasma membrane barrier, is of great importance. The predominant route for nanoparticles to traverse the plasma membrane is through various endocytosis pathways. Nevertheless, nanotechnology has provided new strategies to enhance penetration through the plasma membrane. One type of nanoparticle, namely, single-walled carbon nanotubes (SWCNTs), holds immense potential for diverse biomedical applications due to their biocompatibility upon functionalization, and optical properties, including near-infrared fluorescence within the near-infrared biological transparency window. Specifically, SWCNTs have been utilized to target cells as a vehicle for drug delivery, gene therapy, and as sensors for various intracellular biomarkers. Like other nanoparticles, the main internalization route of SWCNTs into cells is endocytosis, therefore, methods for enhancing the cellular uptake of SWCNTs are of great importance. In this research, we demonstrate a novel approach, repurposing a transfecting reagent, for promoting cell internalization of functionalized SWCNTs. We explore different types of SWCNTs functionalization, namely single-stranded DNA (ssDNA) or polyethylene glycol (PEG)-lipids, and two different cell types, embryonic kidney cells and adenocarcinoma lung tissue cells. We show that internalizing PEGylated functionalized SWCNTs is enhanced in the presence of the transfecting reagent, where the effect is more pronounced for negatively charged lipid-PEG. However, ssDNA-SWCNTs tend to form aggregates in the presence of the transfecting reagent, rendering it unsuitable for promoting internalization. For all cases, cellular uptake is visualized by near-infrared fluorescence microscopy, showing that the SWCNTs are

typically localized within the lysosome. Generally, cellular internalization was higher in the adenocarcinoma cells, thereby paving new avenues for drug delivery and sensing in malignant cells.

Publications

Naamah Levin, Adi Hendler-Neumark, Dotan Kamber, and Gili Bisker, **Enhanced Cellular Internalization of Near-Infrared Fluorescent Single-Walled Carbon Nanotubes Facilitated by a Transfection Reagent**. *J. Colloid Interface Sci.* **2024**, 664 (March), 650–666.



Levin et.al. provide a method for enhancing internalization of PEGylated functionalized single-walled carbon nanotubes (SWCNTs) by different types of cells by utilizing the transfection reagent Lipofectamine Crisprmax. The enhancement was demonstrated with NIR fluorescent imaging of the SWCNTs within the cells, and the SWCNTs were found to be localized primarily in the lysosomes of the cells. It was evident from the research that the enhancement was greater for the malignant adenocarcinoma cells. The findings of the research can promote further research of enhanced bio-sensing bio-imaging and drug delivery systems for cells.

Table of Contents

<i>List of figures</i>	<i>vi</i>
1. Introduction	1
1.1 Cellular internalization of nanoparticles	1
1.2 Single-Walled Carbon Nanotubes (SWCNTs)	2
1.2.1 Structure and properties	2
1.2.2 Functionalization of SWCNTs.....	4
1.3 Transfection reagent induces endocytosis	5
Research goal	7
2 Methods	9
2.1 Single-walled carbon nanotubes (SWCNTs) suspension	9
2.1.1 SWCNTs with ssDNA suspension:.....	9
2.1.2 SWCNTs with PEGylated lipids suspension:	9
2.2 TEM imaging	10
2.3 Zeta potential	10
2.4 Cell culture	11
2.5 Fluorescence spectroscopy	12
2.6 Fluorescence imaging	12
2.7 Image analysis	13
2.8 Cell viability	14
3 Results and Discussions	15
3.1 Characteristics of functionalized SWCNTs pretreated with Lipofectamine Crisprmax	15
3.2 Cellular internalization of functionalized SWCNTs	22
3.3 Intracellular fluorescence imaging of internalized functionalized SWCNTs	37
3.4 Colocalization analysis of internalized SWCNTs with the Lysosomes of the cell	40

3.5 Cell viability.....	44
4 <i>Conclusions</i>	47
<i>References</i>	49
<i>Appendix</i>	70
תקציר	72

List of figures

Figure 1. Scheme of endocytosis mechanisms of nanoparticle cellular internalization.

Figure 2. Different SWCNT chirality structures

Figure 3. SWCNT optical properties

Figure 4. Liposome mechanism for promoting endocytosis.

Figure 5. Schematic illustration of proposed research. Potential enhancement of SWCNTs internalization into cells, with or without utilization of a transfection reagent.

Figure 6. Optical properties of PEG-SWCNTs

Figure 7. Optical properties of (GT)₁₅-SWCNTs

Figure 8. Fluorescence and absorption spectra of different functionalized SWCNTs without and with Lipofectamine Crisprmax

Figure 9. Aggregates in the solution of (GT)₁₅-SWCNT pretreated with Lipofectamine Crisprmax

Figure 10. TEM images of PEG-SWCNTs without and with Lipofectamine Crisprmax.

Figure 11. TEM images of (GT)₁₅-SWCNTs without and with Lipofectamine Crisprmax.

Figure 12. Fluorescence microscopy images of SWCNTs with different types of functionalization internalized in A549 cells without or with Lipofectamine Crisprmax.

Figure 13. Images of A549 cells following overnight incubation with (GT)₁₅-SWCNTs with and without Lipofectamine for different Z positions, with same NIR fluorescence exposure time.

Figure 14. Cell viability of A549 cells following overnight incubation with different quantities of Lipofectamine Crisprmax.

Figure 15. Internalization efficiency of PEG-SWCNTs when pretreated with different quantities of Lipofectamine Crisprmax in A549 cells.

Figure 16. Cluster formation of (GT)₁₅-SWCNTs when pretreated with different quantities of Lipofectamine Crisprmax.

Figure 17. Fluorescence microscopy images of SWCNTs with different types of functionalization internalized in HEK293T cells without or with Lipofectamine Crisprmax.

Figure 18. Z-stacks images of A549 and HEK293T cells following internalization of DSPE-PEG-SWCNTs pretreated with Lipofectamine Crisprmax.

Figure 19. Z-stacks images of A549 and HEK293T cells following internalization of DPPE-PEG-SWCNTs pretreated with Lipofectamine Crisprmax.

Figure 20. Z-stacks images of A549 and HEK293T cells following internalization of (GT)₁₅-SWCNTs.

Figure 21. Marked ROI for the analysis of A549 cells following incubation overnight with DSPE-PEG-SWCNTs pretreated with Lipofectamine Crisprmax.

Figure 22. Images of external aggregates of (GT)₁₅-SWCNTs pretreated with Lipofectamine Crisprmax observed over several internal Z positions of the HEK293T cells.

Figure 23. Intracellular NIR fluorescence intensity of the different functionalized SWCNTs per cell area for two different concentrations with and without Lipofectamine Crisprmax.

Figure 24. Colocalization analysis of the internalized functionalized SWCNTs with lysosomes of A549 cells.

Figure 25. Colocalization analysis of the internalized functionalized SWCNTs with lysosomes of HEK293T cells.

Figure 26. Cell viability after incubation with different functionalized SWCNTs with and without Lipofectamine Crisprmax.

1. Introduction

1.1 Cellular internalization of nanoparticles

The development of various nanoparticles, with dimensions in the same order of magnitude as cell organelles, has fueled the growing interest in cellular biomedical applications, including nano-sensing, imaging, and drug delivery transporters¹⁻³. Cellular uptake of nanoparticles involves traversing the cell plasma membrane barrier, which serves as a protective layer from the external environment^{4,5}. The membrane consists of an overall negatively charged phospholipid bilayer with selective permeability to different molecules and nanoparticles. There are several routes for nanoparticles to enter cells through the membrane, mainly via different endocytosis pathways⁶ (Figure 1). Nanotechnology has provided numerous tools to tailor nanoparticles with structures and functionalizations that can enhance penetration through the plasma membrane and promote cellular internalization⁷⁻⁹.

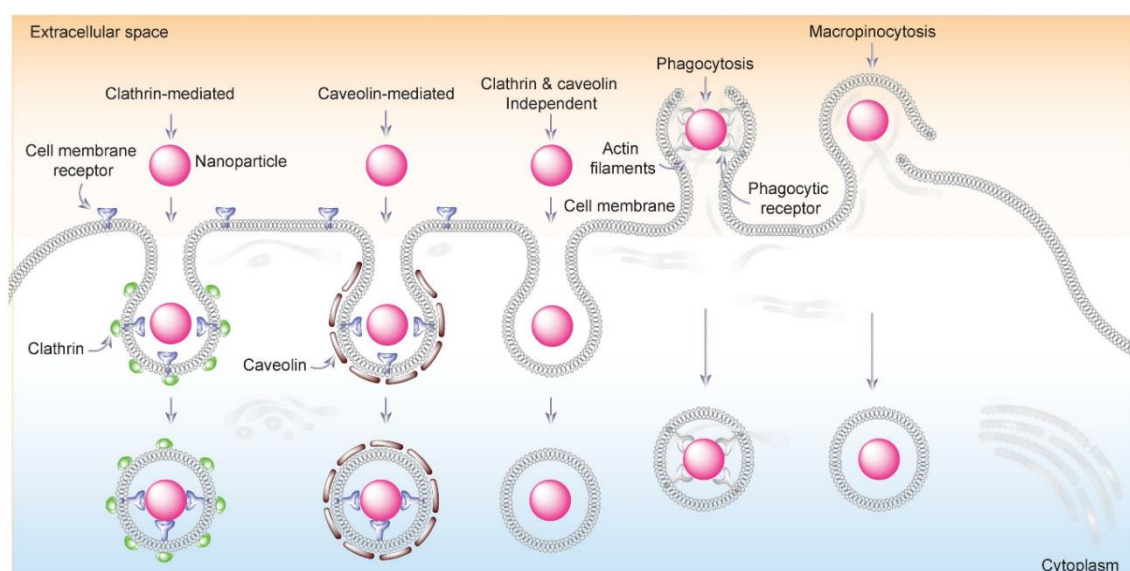


Figure 1. Different endocytosis mechanisms of nanoparticle cellular internalization: clathrin-mediated; caveolin-mediated; clathrin- and caveolin-independent; phagocytosis and macropinocytosis pathways, Adapted from¹⁰.

1.2 Single-Walled Carbon Nanotubes (SWCNTs)

1.2.1 Structure and properties

One promising class of nanoparticles for various biomedical applications on the cellular level, is single-walled carbon nanotubes (SWCNTs). The SWCNTs are comprised of sp²-hybridized carbon atoms, and can be described as rolled-up monolayer sheets of graphene^{11,12}. The SWCNTs' diameter is in the order of 0.4-2 nm, while their length can extend from ~100 nm to several microns, providing a quasi-one-dimensional structure¹³.

The sheet of graphene can roll-up along different vectors as described in Figure 2a. The \vec{a}_1 and \vec{a}_2 represent different basis vectors in the hexagonal graphene lattice. The chirality of the SWCNT is defined as the linear combination of these two vectors, determining the roll-up direction of the sheet of graphene which is described as:

$$\vec{C}_h = n * \vec{a}_1 + m * \vec{a}_2 \quad (1)$$

where n, m are positive integers.

The various chiralities are categorized into three different groups referred to as: "Zigzag" (Figure 2b), "Chiral" (Figure 2c) and "Armchair" (Figure 2d), for $m = 0, n \neq m$ and $n = m$ respectively.

The length of $|\vec{C}_h|$ is the circumference of the cylinder therefore the diameter of the SWCNT can be derived from:

$$D = \frac{|\vec{C}_h|}{\pi} = \frac{a}{\pi} \sqrt{n^2 + m^2 + nm} \quad (2)$$

where a is the length of the vectors \vec{a}_1 and \vec{a}_2 .

The angle of the roll-up vector θ is the angle between \vec{C}_h and \vec{a}_1 and is described as:

$$\theta = \cos^{-1} \left(\frac{2n+m}{2\sqrt{n^2+m^2+nm}} \right) \quad (3)$$

The roll-up vector of the SWCNT, defined by the chiral index (n, m) , affects the density and energy of the electronic state¹⁴, which determines the band gap between the

conduction and valence band, dictating the electrical, and optical properties. The $n = m$, "armchair" structure is metallic, $(n - m) = 3x$, $x \in \mathbb{N}$ is semi-metallic with a small band gap of roughly 1-100 meV whereas any other n, m combinations are semi-conductors^{13,15} with a band gap that varies between 0.5-1 eV, which is negatively correlated with the diameter of the SWCNT.

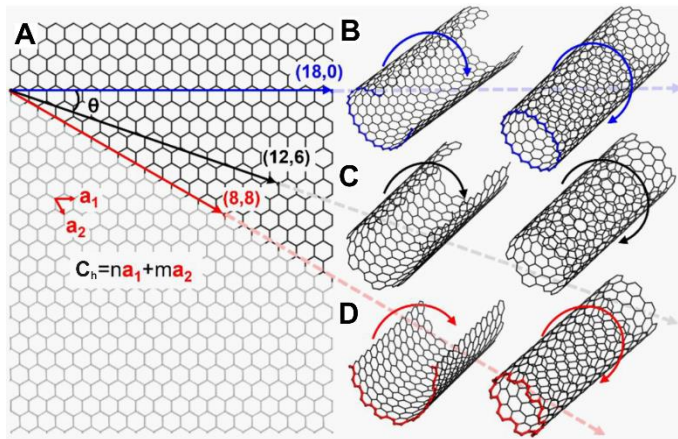


Figure 2. (a) Roll-up vector C_n of a graphene sheet determining the chirality of the SWCNTs, comprised of the linear combination of basis vectors a_1 and a_2 along with the chiral angle θ . Different SWCNT structures (b–d) dictated by the roll-up direction and the length of the vector. (b) "Zigzag" (c) "Chiral" and (d) "Armchair". Adapted with permission from *Acc. Mater. Res.* 2021, 2, 9, 828–841¹⁶. Copyright 2021 American Chemical Society.

The fluorescence of the SWCNT is determined by the electronic band structure. An example of a typical band structure of a semiconducting SWCNT is described in Figure 3a. Light with energy E_{22} is absorbed by the SWCNT, exciting an electron from the valence band V_2 to the conduction band C_2 , thus creating an electron-hole exciton with electrostatic Coulomb force. During relaxation, the electron decays to C_1 due to lattice vibrations, and light with a lower energy E_{11} is emitted, typically in the NIR range.

The bandgap is dictated by the SWCNTs' chirality index (n, m) , consequently different indices correspond to different excitation and emission wavelengths^{15,17} (Figure 3b). The fluorescence of the semiconducting SWCNTs is typically between 900 nm – 1400 nm, coinciding with the transparency window of biological samples (Figure 3c), where autofluorescence, absorption, and scattering are suppressed^{18–22}. Furthermore, SWCNTs

do not photo blink or photo-bleach²³, therefore have a stable fluorescence over a long period of time.

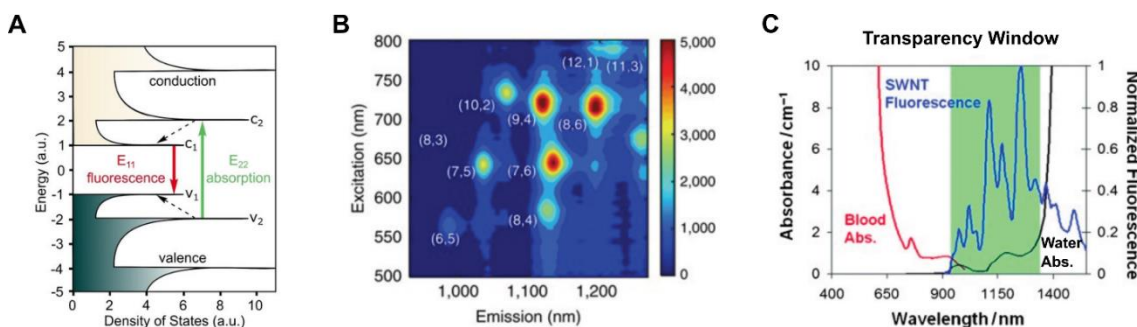


Figure 3. (a) Density of electronic states (DOS) of a semiconducting single-walled carbon nanotube structure. Solid arrows represent the excitation E_{22} ($V_2 \rightarrow C_2$) and emission E_{11} ($C_1 \rightarrow V_1$) transitions; dashed arrows indicate the non-radiative relaxation of electron (in the conduction band) and hole (in the valence band) prior to emission. Adapted from¹⁴. (b) Excitation–emission map of a PEGylated-functionalized SWCNT suspension with the different chiralities marked in white. Adapted from²⁴ (c) Biological Transparency window. SWCNTs fluoresce (blue) primarily in the near-infrared range (820–1600 nm). Blood (red) and water (black) absorbance spectra primarily in the visible regime and second infrared window, respectively. The range of minimal absorbance in biological samples in the near-infrared regime, has minimal interference with SWCNT fluorescence. Adapted from²³.

SWCNTs are hydrophobic in nature, therefore they tend to aggregate in solvents like water¹⁴ due to strong van der Waals forces, which consequently hinders the fluorescence ability of the SWCNTs. The relatively high surface area of the SWCNT can be functionalized²⁵ by suspension with various molecules which provide colloidal stability to the SWCNTs in aqueous environment. Furthermore, SWCNTs were shown to be biocompatible given proper surface functionalization^{7,26–28}. Along with the previously mentioned attributes, SWCNTs became favorable candidates for biomedical imaging^{20,29–33} sensing^{24,25,34–50}, and attractive nano-carriers for drug delivery and gene therapy applications^{51–53}.

1.2.2 Functionalization of SWCNTs

Functionalization of SWCNTs can be achieved with covalent and non-covalent binding⁵⁴. For example, using ssDNA heteropolymers⁵⁵, which organize around the SWCNT in a compact fashion by adsorbing to the SWCNT surface via π - π stacking interactions with the oligonucleotides^{56–58}, or using polyethylene glycol (PEG) adsorbed onto the SWCNT

surface via hydrophobic interactions with the lipid chains^{24,59}. Other functionalizations of SWCNTs include non-covalent adsorption of surfactants^{60,61}, proteins^{25,62}, peptides^{63–67}, peptoids⁶⁸, dendrons⁶⁹, polymers^{70,71}, and more. The heteropolymer that adsorbs onto the SWCNT surface forms a corona phase around the nanotube, mediating the interaction with an analyte^{14,28,72}. The carbon atoms are all located on the external surface of the SWCNT, therefore, an exciton that diffuses along the SWCNT axis is influenced by chemical processes on the external surface¹⁴. Subsequently, upon analyte interaction, the fluorescence emission of the SWCNT can be modified, manifesting a modulation of the intensity or the peak emission wavelength^{25,73,74}.

1.3 Transfection reagent induces endocytosis

Many studies focused on cellular internalization of SWCNTs^{75,76} for bio-sensing^{29,77,78}, bioimaging^{79–85} and drug delivery^{52,53,86}, featuring the impact of SWCNT purity⁸⁷ and aggregations⁸⁴ on the SWCNT fluorescence intensity within the cells. Endocytosis predominantly governs cellular internalization of SWCNTs^{88–90}, where ssDNA functionalized SWCNTs were shown to enter endothelial cells via micropinocytosis⁹¹. Although covalently-functionalized SWCNTs were shown to have high capacity to be internalized by cells⁹², it has been demonstrated that the nanostructure, length, and other types of covalent and noncovalent functionalization of the SWCNT determines the rate of the cellular uptake^{93,94}.

Transfection reagents were designed with the aim of facilitating the translocation of biomolecules, specifically DNA and siRNA/miRNA, into cells by penetrating through the cells' membrane via endocytosis^{95,96}. Amongst the various transfection reagents available, Lipofectamine stands out as the most widely used due to its high transfection efficiency, earning its status as the “gold standard” in the field^{97,98}. Specifically,

Lipofectamine Crisprmax has been identified as the most effective for transporting CAS9 and gRNA, with low cytotoxicity⁹⁹. The transfection mechanism of Lipofection relies on a cationic lipid bilayer that self-assembles with an anionic biomolecule, generating a complex that presents a positive charge, which then binds to the negatively charged cell membrane and releases the payload^{100–102} (Figure 4). While the original application of Lipofectamine is transporting CAS9 protein, DNA and siRNA/miRNA into cells, it has been used for facilitating cellular internalization of other nanoparticles without presenting cytotoxic effects^{103–105}. Despite these accomplishments, the potential of Lipofectamine to enhance the internalization of SWCNTs into cells remains unexplored.

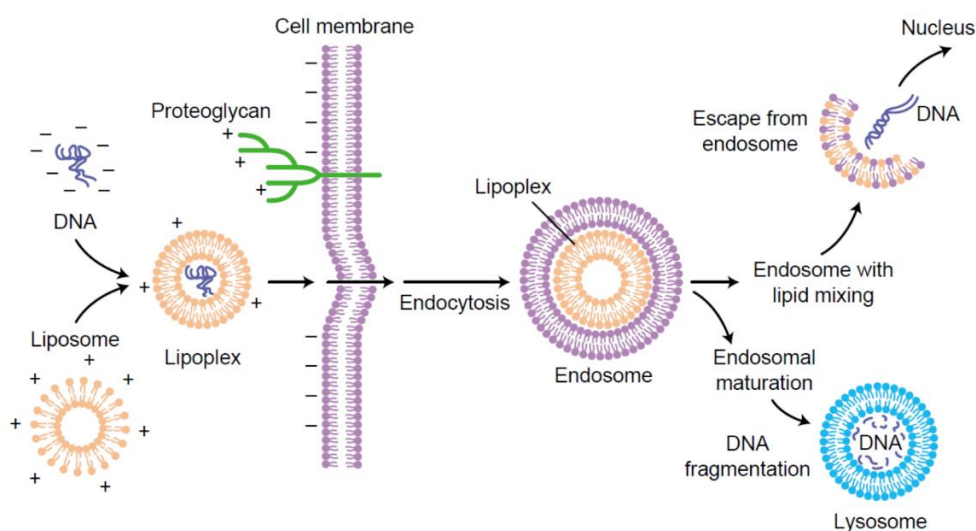


Figure 4. Lipoplex-mediated transfection and endocytosis. A cationic liposome complexed with DNA to create a lipoplex presenting a positive charge to the negatively charged plasma membrane. The complex is then internalized via endocytosis. The DNA can be released from the endosome into the cytoplasm, or alternatively the endosome can mature into a lysosome, where the DNA is degraded. Adapted from¹⁰⁶

Research goal

Our study sets out to explore the potential enhancement of internalization of various functionalized SWCNTs by different types of cells by utilizing the transfection reagent Lipofectamine Crisprmax¹⁰⁷, which was originally designed to enhance the internalization of other biomolecules by cells via endocytosis. The enhancement of the cellular internalization of the functionalized SWCNTs is assessed by evaluating the intensity and location of the internalized SWCNTs recorded by NIR fluorescence imaging (Figure 5). The basis of the research relies on the binding of the positively charged Lipofectamine Crisprmax to the functionalized SWCNT, enabling its penetration through the negatively charged membrane of the cell.

In order to achieve this, we selected three different types of functionalized SWCNTs. Two of them were PEGylated functionalized SWCNTs (PEG-SWCNTs) with different electrical charges, namely DPPE-PEG-SWCNT without a charge and DSPE-PEG-SWCNT with a negative charge, while the third one was functionalized with a ssDNA, namely (GT)₁₅-SWCNT. We chose two different types of cells to investigate the enhancement of the cellular internalization of the functionalized SWCNTs with Lipofectamine Crisprmax, HEK293T human embryonic kidney epithelial cells and A549 adenocarcinoma alveolar epithelial human cells, providing diverse representation of cellular internalization of the different functionalized SWCNTs.

The main motivation for this research is to enable the use of functionalized SWCNTs for various biomedical applications on the cellular level, such as SWCNT-based carriers for drug delivery and bio-sensing, which otherwise would be inadequate due to the low cellular uptake.

We set out to investigate the destination of the various internalized SWCNTs for the different cells by using fluorescent dyes for the cellular organelles in the visible range, which do not overlap with the NIR SWCNT fluorescence, to further learn of the nature of internalization of the SWCNTs. Lastly, we wanted to ensure that for low concentrations of the various functionalized SWCNTs with and without Lipofectamine Crisprmax there were no adverse cytotoxic effects.

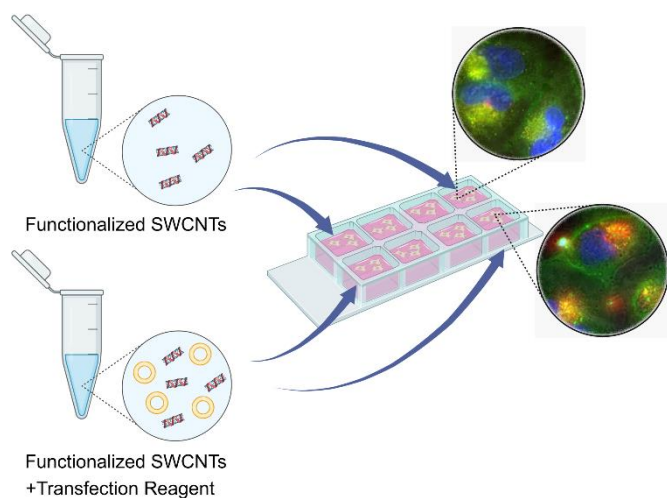


Figure 5: Schematic illustration of SWCNTs internalization into cells with or without the transfection reagent, Lipofectamine Crisprmax. A SWCNTs suspension with or without the transfection reagent is added to the media of cultured cells, incubated overnight, and imaged in visible and NIR fluorescence microscopy. The membrane, nucleus, and lysosome are labeled with standard fluorescent dyes in the visible range (green, blue, and yellow, respectively), whereas the red indicates the SWCNT fluorescence in the NIR. The transfection reagent enhances SWCNT internalization by the cells. Created with BioRender.com.

2 Methods

2.1 Single-walled carbon nanotubes (SWCNTs) suspension

2.1.1 SWCNTs with ssDNA suspension:

1 mg of HiPCO SWCNTs (NanoIntegris, carbon purity >80 wt% (95 atom%)) was suspended with 2 mg of single-stranded DNA (ssDNA) with the sequence (GT)₁₅ (Integrated DNA Technologies) in 0.1 M NaCl using an ultrasonic bath sonicator (Elma P-30H, 80 Hz for 10 min), followed by two rounds of direct tip sonication (QSonica Q125, 3 mm tip, 4 W for 20 min) while in an ice bath. The suspension was then centrifuged twice for 90 min at 16,100 rcf in order to separate the individually suspended SWCNTs from aggregates and impurities. After each centrifugation, 80% of the supernatant was collected, and the residue was discarded. The absorption spectrum of the SWCNT suspension was acquired by a UV–vis–NIR spectrophotometer (Shimadzu UV-3600 PLUS), where distinguishable peaks indicated a successful suspension. The concentration of suspended SWCNT was determined according to the extinction coefficient of $\epsilon_{632\text{nm}} = 0.036 \text{ L mg}^{-1} \text{ cm}^{-173}$, indicating that approximately 23% of the SWCNTs remained in the colloidal suspension.

2.1.2 SWCNTs with PEGylated lipids suspension:

We functionalized the SWCNTs with PEGylated lipids: 1,2-dipalmitoyl-sn-glycero-3-phosphoethanolamine-N-[methoxy(polyethylene glycol)-5000] (DPPE-PEG) and 1,2-distearoyl-sn-glycero-3-phosphoethanolamine-N-[carboxy(polyethylene glycol)-2000] (DSPE-PEG) (Avanti Polar Lipids) in the following method: 20 mg of HiPCO SWCNTs (NanoIntegris, carbon purity >80 wt% (95 atom%)) was initially suspended with 2 wt % sodium cholate (SC) (Sigma Aldrich), using an ultrasonic bath sonicator (80 Hz for 10 min, Elma P-30H), followed by two rounds of direct tip sonication (QSonica Q125, 6 mm tip, 12 W for 30 min) while in an ice bath. The suspension was then ultracentrifuged (41300 rpm for 4 h, OPTIMA XPN-80) to separate the individually

suspended nanotubes from aggregates and other impurities. 80% of the supernatant was collected, and the residue was discarded. According to the suspension concentration determined by the UV–vis–NIR spectrophotometer, as described earlier, approximately 8% of the SWCNTs remained in the colloidal suspension. Subsequently, a solution of 40 mg L⁻¹ SC-SWCNTs with 2 mg mL⁻¹ PEGylated lipids was dialyzed against water for 7 days with multiple water exchanges, to replace the small surfactant molecules with the PEG-lipid derivatives on the nanotube surface.

2.2 TEM imaging

Samples of 50 µL of the different functionalized SWCNT suspension solutions were prepared by dilution in deionized (DI) water. Some of the samples were incubated for 2 h with 0.75 µl Lipofectamine Crisprmax solution (Thermo Fisher) diluted in either 50% OptiMEM medium (Gibco) or deionized (DI) water to the same volume of 50 µL, such that the final SWCNT concentration of all samples was 2 mg L⁻¹. 30 µL of each type of functionalized SWCNT suspension without and with Lipofectamine Crisprmax were applied to a carbon-coated grid. The grid was blotted with filter paper to remove excess solution and subsequently stained with 30 µL of 2% (w/v) uranyl acetate solution. After the removal of excess stain solution, the grid was left to air-dry. The stained samples were imaged with a JEM-1400plus TEM (JEOL, Japan) operating at 80 kV. Images were recorded by a camera (SIS Megaview III) and TEM imaging platform (iTEM, Olympus).

2.3 Zeta potential

The Zeta potential was acquired for the functionalized SWCNT suspensions after dilution in DI water to 10 mg L⁻¹, 20 mg L⁻¹, and 20 mg L⁻¹ for DPPE-PEG-SWCNTs, DSPE-PEG-SWCNTs, and (GT)₁₅-SWCNTs, respectively. For Zeta potential measurements of the functionalized SWCNTs pretreated with Lipofectamine Crisprmax, 1 mL vials of the

different functionalized SWCNT suspensions diluted to 5 mg L^{-1} in DI water were prepared. Subsequently, $37.5 \text{ }\mu\text{l}$ of Lipofectamine Crisprmax was added to the vials, and incubated for at least 30 min prior to measuring the surface charge. The Zeta potential measurements were performed by the Malvern Zetasizer Nano ZS device (Malvern Instruments, UK) with 3 measurements of 15-30 runs each and evaluated with Zetasizer software.

2.4 Cell culture

HEK293T cells were kindly received from Dr. Ines Zucker (Tel Aviv University, Israel). A549 cells, at an early passage, were kindly received from Prof. David Gurwitz (Tel Aviv University, Israel). The cells were cultured under standard incubation conditions (at 37°C , $5\% \text{ CO}_2$) with Dulbecco's modified Eagle medium (DMEM) supplemented with 10% fetal bovine serum (FBS), 1% penicillin-streptomycin, and 1% L-glutamine (complete DMEM). For live cell fluorescence imaging, the cells were seeded in 8 well μ -Slide, $300 \text{ }\mu\text{l}$ per well, treated with Poly-L-Lysine (Ibidi). The seeded cells reached roughly 80% confluency on the day of the experiment (3 to 4 days after plating). For SWCNTs internalization experiments, up to 24 h prior to imaging, different quantities of suspended SWCNTs were diluted in $25 \text{ }\mu\text{l}$ OptiMEM medium (Gibco) and added to the wells, such that the final concentration of the SWCNTs was 0.3 mg L^{-1} or 0.15 mg L^{-1} , depending on the experiment. In some experiments, as detailed in the text, in accordance with the recommendation in the protocol of the manufacturer, $0.75 \text{ }\mu\text{l}$ (unless stated otherwise) of Lipofectamine Crisprmax solution (Thermo Fisher), was added to the OptiMEM with the SWCNTs. The SWCNTs with the Lipofectamine Crisprmax were incubated at room temperature for 10 min prior to adding the SWCNTs to the wells without removal of excess Lipofectamine Crisprmax. The cells were incubated with the SWCNTs for up to 24 hr in standard incubation conditions. Before imaging, the cells were washed $2\times$, and

fresh clear media with fluorescent dyes (Hoechst 1 $\mu\text{g mL}^{-1}$, LysoTracker 60 nM, and CellMask 1 \times , all purchased from Thermo Fisher) were added and incubated for at least 15 min.

2.5 Fluorescence spectroscopy

Fluorescence emission spectra of the SWCNTs were acquired in triplicates in a 96-well-plate mounted on an inverted microscope (Olympus IX73), which was coupled to a spectrograph (Spectra Pro HRS-300, Teledyne Princeton Instruments) with a slit-width of 500 μm and a grating (150 g mm^{-1}), and recorded by a liquid-nitrogen cooled InGaAs-detector (PylonIR, Teledyne Princeton Instruments), with 3 s exposure time. The samples were excited with a super-continuum white-light laser (NKT-photonics, Super-K Extreme) with a bandwidth filter (NKT-photonics, Super-K varia, $\Delta\lambda=20$ nm). The excitation wavelength was $\lambda_{\text{ex}}=730$ nm with an intensity of 20 mW at the sample plane. Excitation-emission maps were acquired with an excitation wavelength range of 420 nm – 840 nm, in steps of 2 nm.

2.6 Fluorescence imaging

Images were captured with an inverted fluorescence microscope (Olympus IX83) with different magnifications: 20 \times , 0.7 NA (Plan FL), and 100 \times , 1.3 NA (Plan FL). Fluorescence in the visible range was excited with an LED illumination system (CoolLED, pE4000) by selecting the channel corresponding to the desired fluorescent dye (365 nm; 460 nm; or 635 nm). The fluorescence image was obtained using three different filter cubes: DAPI (Chroma, 49000-ET-DAPI), GFP (Chroma, 49002-ET-EGFP (FITC/Cy2)) and Cy5 (Chroma, 49009-ET-Cy5), recorded by an EMCCD camera (Andor, iXon Ultra 888) using VisiView software (Visitron Systems GMBH). The SWCNTs were excited by a 730 nm CW laser (MDL-MD-730-1.5 W, Changchun New

Industries). The laser excitation light was directed to the sample by a dichroic mirror (900 nm long-pass, Chroma), and the NIR emission of the SWCNTs was detected with an InGaAs camera (Raptor, Ninox 640 VIS-NIR) after a 900 nm long-pass emission filter (Chroma, ET900lp) using Micro-Manger software (see https://micro-manager.org/Citing_Micro-Manager).

2.7 Image analysis

All images were processed with ImageJ, and MATLAB. The EMCCD camera and the InGaAs camera have different pixel sizes, different chip dimensions, and slight rotational and axial misalignment. The overlay of the images captured from the two cameras was done by adjusting the number of pixels, pixel sizes, and orientation. The overlay parameters of the images were determined by maximization of the 2D autocorrelation of identical images captured by both cameras. The images were then rotated and cropped to the desired size and position.

For determining the fluorescence intensity of the SWCNTs internalized by cells, the perimeters of the cell were manually selected in ImageJ, according to the perimeters of the stained membranes of the cells captured by the visible camera. The selections marked the region of interest (ROI), which was then overlaid with the NIR image captured by the InGaAs camera after it was fitted to the proper dimensions and orientation. The intensity within the ROI was calculated in ImageJ, and the data was then processed in MATLAB.

Only cells for which over 80% of the image of the cell was captured, were selected for the analysis.

For the colocalization analysis of the internalized SWCNTs with the lysosomes of the cells, we manually marked the perimeter of the cells which internalized SWCNTs as the

ROIs. The colocalization coefficients were analyzed with the BIOP JACoP plugin in ImageJ for the different ROIs using the Otsu threshold.

2.8 Cell viability

In order to determine the cell viability, the cells were stained with $1 \mu\text{g mL}^{-1}$ Hoechst, which permeates the nuclease and binds to adenine-thymine (A-T), and 500 nM Propidium iodide (PI) stain, which detects dead cells by binding to the nuclease with ruptured membrane. The cells were imaged with the inverted fluorescence microscope (Olympus IX83) with a magnification of $20\times$ driven by VisiView software. The cells were excited with a LED illumination system (CoolLED, pE4000) by selecting the channel corresponding to the desired fluorescent dye (365 nm or 525 nm). The fluorescence was acquired with an EMCCD camera (Andor, iXon Ultra 888) by using different filter cubes DAPI (Chroma, 49000-ET-DAPI) or mCherry (Chroma, 49008-ET-mCherry, Texas Red) for imaging the live and dead cells respectively.

To assess the toxicity of the SWCNTs, the relative number of dead cells with SWCNTs was compared to the relative number of dead cells without SWCNTs.

3 Results and Discussions

3.1 Characteristics of functionalized SWCNTs pretreated with Lipofectamine Crisprmax

We explored three different types of functionalizations of SWCNTs for internalization into cells (Appendix, Table A1). Two out of the three were derivatives of PEGylated lipids, namely, DPPE-PEG (5 kDa), which has no charge, and DSPE-PEG (2 kDa) Carboxylic Acid with an overall negative charge, and the third type was single-stranded DNA, (GT)₁₅. The hydrophobic end of the PEGylated lipid adheres to the exterior surface of the SWCNT, while the hydrophilic end extends in the solution, forming a somewhat bulky corona⁵⁹, whereas the ssDNA helically wraps around the SWCNT in a compact fashion^{56,108,109}. The functionalization of the SWCNTs with the PEGylated lipids was performed by surfactant exchange of SWCNT suspended in sodium cholate (SC), via dialysis in the presence of DPPE-PEG or DSPE-PEG, to remove the SC and to allow for the PEGylated-lipids to bind to the SWCNT surface instead. The suspension was then centrifuged, and the supernatant was collected for the experiments. The DPPE-PEG-SWCNT and the DSPE-PEG-SWCNT suspensions both demonstrated redshifts in their absorption spectra recorded in the UV–vis–NIR spectrophotometer (Figure 6a and 6b, respectively), and bright fluorescent emission peaks, corresponding to the different chiralities of the SWCNTs in the suspension (Figure 6c and 6d, respectively).

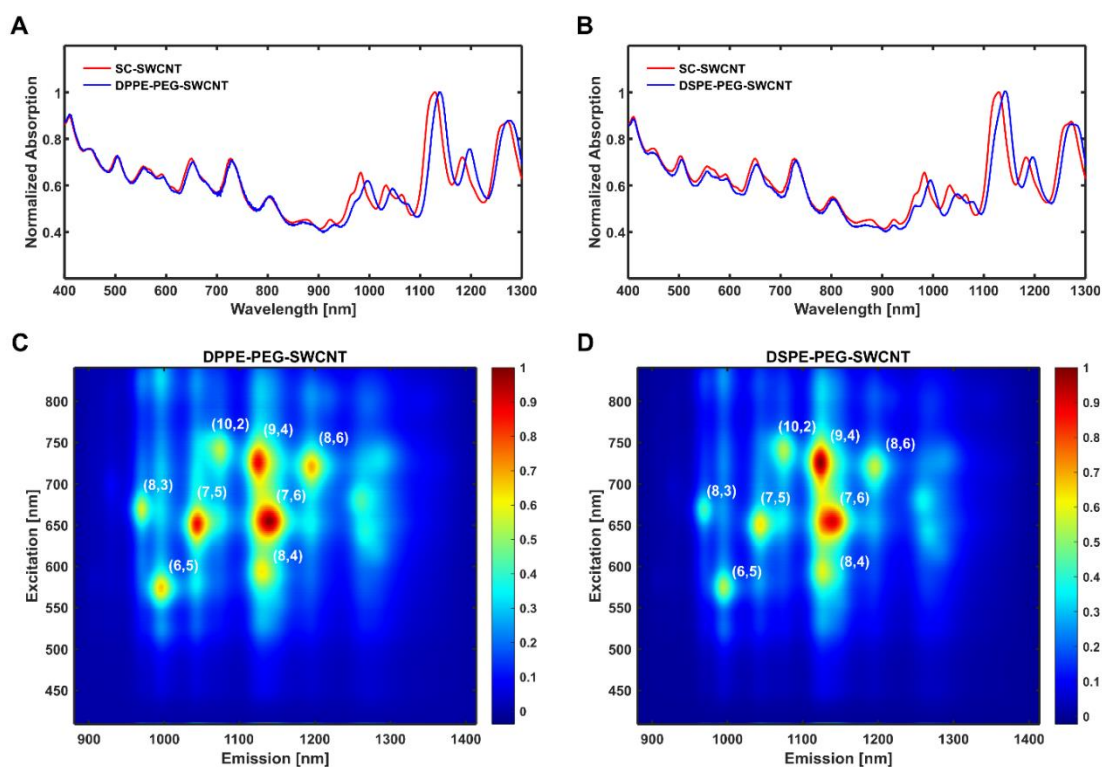


Figure 6. Optical properties of PEG-SWCNTs. (a) and (b) Normalized absorption spectra of the parent SC-SWCNT suspension (red) and (a) DPPE-PEG-SWCNT suspension (blue), and (b) DSPE-PEG-SWCNT suspension (blue), following dialysis. The red shift in the PEG-SWCNT suspension spectra indicates the successful exchange of the SC by the PEGylated lipid on the SWCNT exterior surface. (c) Excitation-emission maps with bright fluorescence peaks of the various SWCNT chiralities of DPPE-PEG-SWCNT and (d) DSPE-PEG-SWCNT.

The functionalization with $(GT)_{15}$ ssDNA was performed by direct sonication of the SWCNT with $(GT)_{15}$, which then underwent centrifugation twice, where 80% of the supernatant was collected each time to discard aggregates and impurities. The successful suspension was similarly characterized by the absorption peaks (Figure 7a) and the bright fluorescent peaks (Figure 7b).

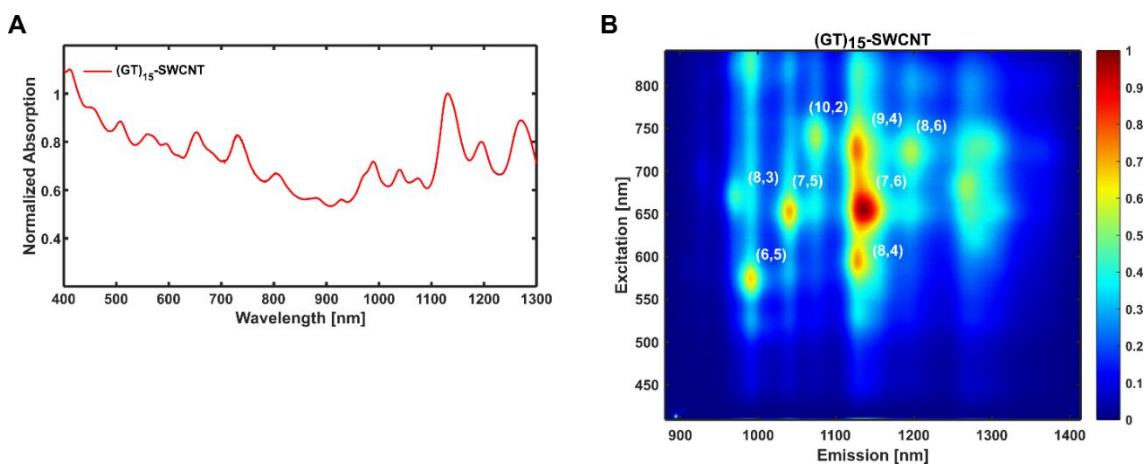


Figure 7. Optical properties of (GT)₁₅-SWCNTs. (a) Normalized absorption spectra of (GT)₁₅-SWCNT suspension presenting absorption peaks indicative of a successful (GT)₁₅-SWCNTs suspension. (b) (GT)₁₅-SWCNTs excitation-emission map presenting bright fluorescence peaks of the various chiralities.

We set out to investigate the cellular uptake of the different types of functionalized SWCNTs, and a possible enhancement of the uptake using Lipofectamine Crisprmax. Lipofectamine is composed of a cationic lipid bilayer designed to encapsulate negatively charged nanoparticles efficiently, to be attracted to the negatively charged cell membrane and promote endocytosis^{100,101,110}, where Lipofectamine Crisprmax specifically demonstrated low cell toxicity⁹⁹. While Lipofectamine Crisprmax is widely used for delivering exogenous strands of DNA or RNA into cells for gene editing purposes^{111–113}, we decided to explore this technology for promoting endocytosis for functionalized SWCNTs.

For cellular internalization experiments, the SWCNTs (1 mg L⁻¹) were pretreated with 7.5 μ l Lipofectamine Crisprmax, and incubated with the cells overnight before imaging. We, therefore, tested the effects of Lipofectamine Crisprmax on the optical properties of the different functionalized SWCNTs, by acquiring the absorption and fluorescence spectra of the SWCNTs with and without Lipofectamine Crisprmax at the time points $t = 0$ h and $t = 24$ h. The fluorescence spectra of DPPE-PEG-SWCNT and DSPE-PEG-SWCNTs (Figures 8a and 8b) were not affected by Lipofectamine Crisprmax, showing similar emission spectra for both time points. In contrast, the intensity of the fluorescence

of (GT)₁₅-SWCNTs (Figure 8c) was lower with Lipofectamine Crisprmax for both time points compared to the (GT)₁₅-SWCNTs without Lipofectamine Crisprmax.

While the absorption spectra of DPPE-PEG-SWCNT and DSPE-PEG-SWCNT (Figures 8d and 8e) were similar with and without Lipofectamine Crisprmax over the course of 24 hours, the absorption of (GT)₁₅-SWCNTs (Figure 8f) was higher mainly in the UV and visible range, when pretreated with Lipofectamine Crisprmax at both time points. Moreover, at $t = 24$ h, the (GT)₁₅-SWCNTs pretreated with Lipofectamine Crisprmax presented a slight broadening of the absorbance peaks.

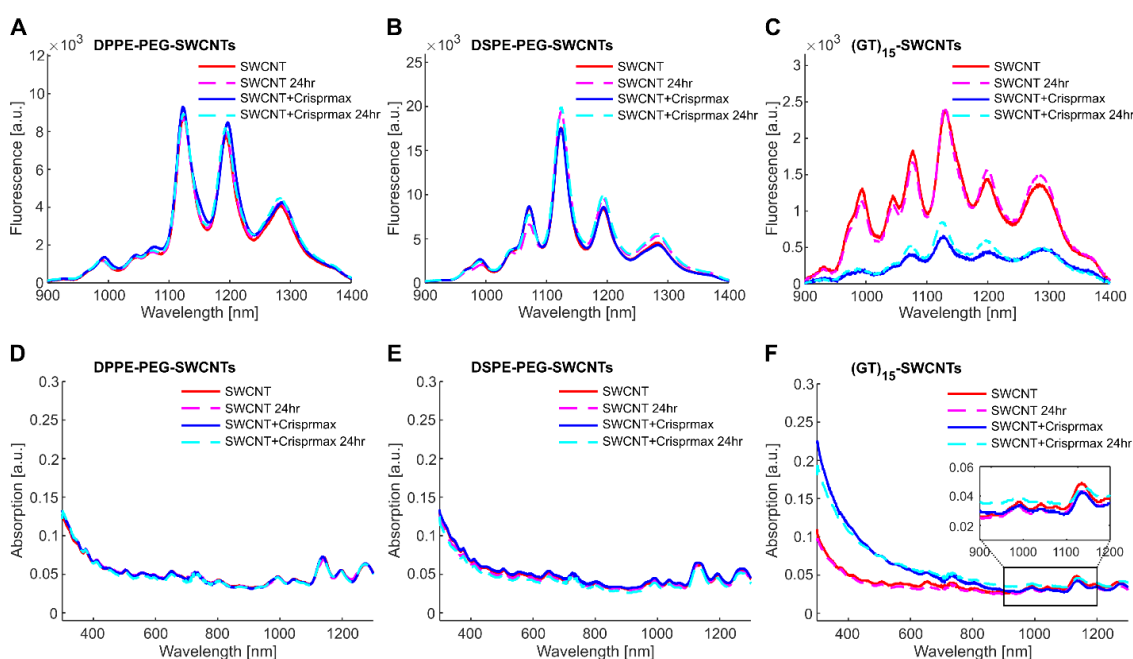


Figure 8. Fluorescence spectra acquired under 730 nm excitation and absorption spectra of different functionalized SWCNTs (1 mg L^{-1}) without Lipofectamine Crisprmax at times $t = 0$ h (red line), and $t = 24$ h (dashed magenta line), and with Lipofectamine Crisprmax at times $t = 0$ h (solid blue line), and $t = 24$ h (dashed cyan line). Fluorescence of (A) DPPE-PEG-SWCNTs in water, (B) DSPE-PEG-SWCNTs in water, and (C) (GT)₁₅-SWCNTs in 0.1 M NaCl. Absorption spectra of (D) DPPE-PEG-SWCNTs in water, (E) DSPE-PEG-SWCNTs in water, and (F) (GT)₁₅-SWCNTs in 0.1 M NaCl.

Furthermore, after 24 h, clusters of (GT)₁₅-SWCNTs was observed in the solution (Figure 9). The decrease in the fluorescence intensity, along with the increase and broadening of the absorption, can therefore be attributed to partial (GT)₁₅-SWCNTs aggregation and to a reduced colloidal stability^{83,84,114,115} resulting from the interaction with Lipofectamine

Crisprmax, whereas the PEGylated lipid functionalized SWCNT suspensions were not affected in that manner by the Lipofectamine Crisprmax.

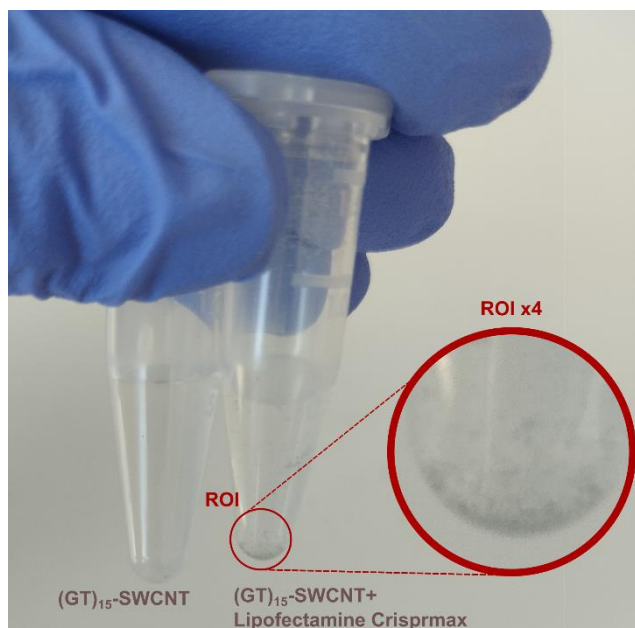


Figure 9. Samples of 1 mg L^{-1} $(\text{GT})_{15}$ -SWCNTs were incubated overnight in 0.1 M NaCl solution without (left) and with (right) $7.5 \text{ }\mu\text{l}$ Lipofectamine Crisprmax. In the latter case, visible SWCNT aggregates were observed in the solution.

We further explored the different functionalized SWCNTs and the effects of Lipofectamine Crisprmax on their structure using transmission electron microscopy (TEM), where we could visualize the individual functionalized SWCNTs and better understand the mechanism of the interaction between the SWCNT and the Lipofectamine Crisprmax. In representative TEM images (Figure 10), DPPE-PEG-SWCNTs and DSPE-PEG-SWCNTs presented similar structures and dimensions of approximately $3 \text{ nm} - 6 \text{ nm}$ in diameter and several hundreds of nanometers in length. Following the incubation of the two different PEG-SWCNTs with Lipofectamine Crisprmax for several hours prior to imaging, the DPPE-PEG-SWCNTs and DSPE-PEG-SWCNTs maintained the same structure, yet round clusters of approximately 50 nm in diameter were visible along the length of the SWCNTs. We hypothesize that these clusters are molecules of Lipofectamine Crisprmax since they show similar morphology to previous TEM findings¹¹⁶. Furthermore, we note that PEG-SWCNTs, following incubation with

Lipofectamine Crisprmax, do not fold to a compact structure completely encapsulated within the Lipofectamine Crisprmax.

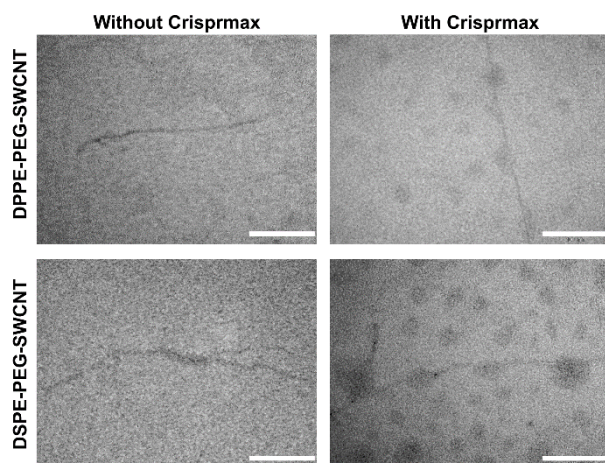


Figure 10. TEM images of PEG-SWCNTs (2 mg L^{-1}) without and with Lipofectamine Crisprmax in water. Scale bars for all images are 100 nm. Top row: DPPE-PEG-SWCNTs, and bottom row: DSPE-PEG-SWCNTs. Left column: PEG-SWCNTs without Lipofectamine Crisprmax, and right column: PEG-SWCNTs following 2 h incubation with Lipofectamine Crisprmax. The structure of both types of PEG-SWCNT appears to be slightly flexible, with a diameter in the range of 3 nm - 6 nm and a length of several hundreds of nanometers. Following incubation with Lipofectamine Crisprmax, the PEG-SWCNTs retain similar dimensions and form, with the addition of spherical structures along the length of the SWCNT with a diameter of approximately 50 nm, attributed to molecules of Lipofectamine Crisprmax.

We additionally imaged $(\text{GT})_{15}$ -SWCNTs without and with Lipofectamine Crisprmax. In representative TEM images (Figure 11), $(\text{GT})_{15}$ -SWCNTs presented similar dimensions to those of the PEG-SWCNTs, approximately 2 nm – 6 nm in diameter and several hundreds of nanometers in length. However, after the incubation with Lipofectamine Crisprmax, large clusters with some aggregated SWCNTs were visible as an entangled network of nanotubes, which could explain the decrease of fluorescence intensity (Figure 8c) and the broadening of the absorbance peaks (Figure 8f).

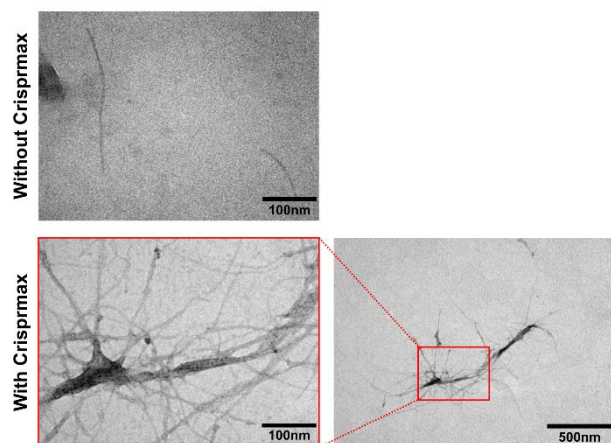


Figure 11. TEM images of (GT)₁₅-SWCNTs (2 mg L⁻¹) without and with Lipofectamine Crisprmax. Top image: (GT)₁₅-SWCNTs without Lipofectamine Crisprmax. Bottom row: (GT)₁₅-SWCNTs following 2 h incubation with Lipofectamine Crisprmax in 50% OptiMEM in two different magnifications. The dimensions of the (GT)₁₅-SWCNTs is in the range of 2 nm - 6 nm in diameter, and several hundreds of nanometers in length. Following the incubation with Lipofectamine Crisprmax, large clusters and an entangled network of SWCNTs are visible, with some aggregation within the cluster.

To further characterize the functionalized SWCNTs without and with Lipofectamine Crisprmax, we took Zeta potential measurements in order to determine their surface charge. The Zeta potential of DPPE-PEG-SWCNTs, DSPE-PEG-SWCNTs, and (GT)₁₅-SWCNTs was -5.2 ± 6 mV, -43 ± 6 mV, and -35 ± 13 mV, respectively, as expected for the neutral DPPE-PEG-SWCNTs, and the negatively charged DSPE-PEG-SWCNTs and (GT)₁₅-SWCNTs. Following the incubation of the different functionalized SWCNTs with Lipofectamine Crisprmax, their Zeta potential values were 1.8 ± 3.6 mV, -22 ± 7 mV, and -37 ± 5.5 mV for the DPPE-PEG-SWCNTs, DSPE-PEG-SWCNTs, and (GT)₁₅-SWCNTs, respectively. It is apparent that the Lipofectamine Crisprmax treatment resulted in the addition of positive charges to the surface of the PEGylated functionalized SWCNTs, not necessarily resulting in an overall positive charge. These findings further support our conclusion based on the TEM images (Figure 10) that Lipofectamine Crisprmax binds to the PEGylated functionalized SWCNTs without fully encapsulating them, such that part of the SWCNT surface, either neutral or negatively charged, is still exposed to the surrounding solution. For the case of (GT)₁₅-SWCNTs with Lipofectamine Crisprmax, the mean Zeta-potential value showed a slight decrease, still within the

standard deviation range; however, the entangled cluster structures of the (GT)₁₅-SWCNTs with the Lipofectamine Crisprmax (Figure 11) might have influenced the measurement results.

3.2 Cellular internalization of functionalized SWCNTs

Two different cell lines were selected, namely A549 human adenocarcinoma epithelial cells originating from cancerous lung tissue, and HEK293T human embryonic kidney cells. The A549 cells have been the focus of numerous studies on anti-malignancy drug delivery using nanoparticle carriers^{117–119}, including nanoparticle-mediated delivery of doxorubicin^{117,120}, dual drug delivery nanoparticles to improve chemotherapy^{121,122}, and studies of the endocytosis mechanism for nanoparticles uptake to enhance drug delivery¹²³. The HEK293T cells are an excellent model for transfection¹²⁴, and therefore, have been extensively used for the production of recombinant proteins^{125–127} and viral vectors^{128,129}. Owing to their high transfection efficiency, the HEK293T cells are widely researched with transfection reagents, specifically with Lipofectamine Crisprmax^{99,130,131}. The two different cell types were incubated overnight with 0.3 mg L⁻¹ of each of the three types of functionalized SWCNTs under standard incubation conditions. In addition, similar cultures of each cell type were incubated overnight in the presence of SWCNTs that were pretreated with Lipofectamine Crisprmax. The following day, the cells were stained with different fluorescent dyes for the nuclei, lysosome, and cell membrane, to better visualize the destination of the SWCNTs within the cells. Subsequently, the live cells were imaged in a visible and NIR dual channel fluorescence microscope, where the images taken by the NIR camera were overlaid on top of the brightfield and visible fluorescence images taken by an EMCCD.

The internalization of the different functionalized SWCNTs by the A549 cells can be seen in the representative images presented in Figure 12. Comparing the uptake of DPPE-PEG-

SWCNT by the A549 cells (Figure 12a) with the uptake of DPPE-PEG-SWCNT in the presence of Lipofectamine Crisprmax (Figure 12b), it is evident that internalization with Lipofectamine Crisprmax is more efficient. The cells that internalized the DPPE-PEG-SWCNT without Lipofectamine Crisprmax were very scarce and mostly had only a single NIR fluorescence spot within them. In contrast, when the DPPE-PEG-SWCNTs were pretreated with Lipofectamine Crisprmax and then incubated with the cells, the vast majority of the cells internalized the DPPE-PEG-SWCNTs, and furthermore, each cell had several fluorescence spots of internalized SWCNT particles. It is evident from the overlay of the images that most of the SWCNTs were located in the lysosomes (Figure 12b).

Similar to DPPE-PEG-SWCNTs, the DSPE-PEG-SWCNTs uptaken by the A549 cells were mostly located within the lysosomes as well, where the uptake was more efficient for SWCNTs pretreated with Lipofectamine Crisprmax, presenting multiple NIR fluorescence spots in each cell (Figure 12c and 12d).

For the PEGylated functionalized SWCNTs without the Lipofectamine Crisprmax, we observed minimal uptake by the cells of both the DPPE-PEG-SWCNTs and the DSPE-PEG-SWCNTs, suggesting that the difference in molecular weight of the PEG chains did not have a significant influence on the internalization efficiency. On the other hand, for the PEGylated functionalized SWCNTs pretreated with Lipofectamine Crisprmax, the DSPE-PEG-SWCNTs exhibited higher fluorescence compared to DPPE-PEG-SWCNTs, which can be partially attributed to the brighter fluorescence of the DSPE-PEG-SWCNT compared to the fluorescence of DPPE-PEG-SWCNT (Appendix, Figure A1).

The internalization of (GT)₁₅-SWCNTs in A549 cells (Figure 12e) was very effective, and more efficient compared to both cases of the PEGylated functionalized SWCNTs, as apparent from the larger number of NIR fluorescence spots in the cells and the lower exposure time required for the NIR images, despite the much brighter fluorescence of the

PEGylated functionalized SWCNTs compared to the (GT)₁₅-SWCNTs (Appendix, Figure A1). In light of a recent study that demonstrated the contribution of the compactness of DNA nanostructures to their uptake by cells⁸, the efficient internalization of (GT)₁₅-SWCNTs could be attributed to the compact corona phase of the ssDNA around the SWCNT resulting from π - π interaction between the nucleobases and the nanotube surface^{56,132}. In contrast, PEGylated functionalized SWCNTs have a more cumbersome structure due to the large hydrophilic PEG corona around the SWCNTs, as only the hydrophobic lipid chains are bound to the SWCNT surface⁵⁹. The (GT)₁₅-SWCNTs were generally located in the lysosome area of the cells, similar to the PEGylated functionalized SWCNTs. These findings coincide with previous studies showing that ssDNA-SWCNTs enter the cell via endocytosis^{29,89,91,133}, since the lysosome is part of the endocytosis pathway. Furthermore, it has been reported that nanoparticles were delivered to the lysosome in A549 cells via macropinocytosis¹³⁴, which could also explain the SWCNT location within the lysosome of the cells.

In contrast to the PEGylated-lipid functionalized SWCNT, (GT)₁₅-SWCNTs internalization was not enhanced by Lipofectamine Crisprmax (Figure 12f). Furthermore, it was evident that the interaction of the (GT)₁₅-SWCNTs with Lipofectamine Crisprmax induced clustering of the SWCNTs, resulting in large NIR fluorescence spots which were captured within focal planes near the top surface of the cell, manifested in the smaller cells circumference appearing in focus in the membrane channel (Figure 12f), compared to the larger membranes circumference for the (GT)₁₅-SWCNTs without Lipofectamine Crisprmax (Figure 12e) or the PEGylated SWCNTs (Figures 12a-d). The (GT)₁₅-SWCNTs pretreated with Lipofectamine Crisprmax were imaged in a relatively low exposure time due to the large emitting clusters which were found in random locations with respect to the cell's organelles.

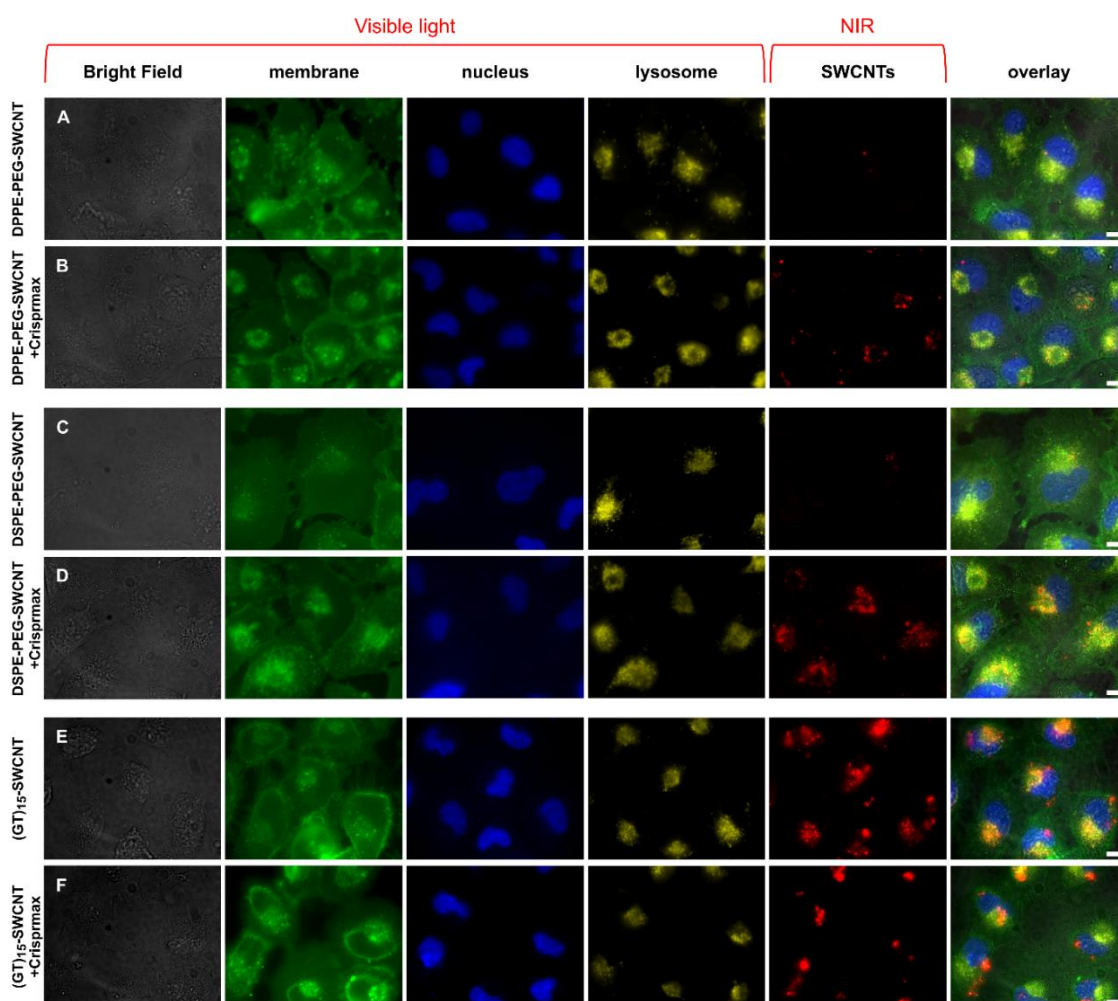


Figure 12. Fluorescence microscopy images of SWCNTs (0.3 mg L^{-1}) with different types of functionalization internalized in A549 cells without or with Lipofectamine Crisprmax. The cells were stained with fluorescent dyes: CellMask (green) for the membrane, Hoechst 33258 (blue) for the nuclei, and LysoTracker (yellow) for the lysosome. The red indicates the NIR fluorescence of the internalized SWCNTs within the cells. The columns from left to right: bright field images, the visible fluorescence channels of the membrane, nucleus, lysosomes, the NIR fluorescence channel of the SWCNTs, and the overlay of all the different fluorescence images, in the visible and NIR. The images were obtained using a $100\times$ objective. The scale bars for all the images are $10 \mu\text{m}$. (A) Internalization of DPPE-PEG-SWCNTs (800 ms exposure time in the NIR) without Lipofectamine Crisprmax and (B) with Lipofectamine Crisprmax (800 ms exposure time in NIR). (C) Internalization of DSPE-PEG-SWCNTs (800 ms exposure time in NIR) without Lipofectamine Crisprmax and (D) with Lipofectamine Crisprmax (400 ms exposure time in NIR). (E) Internalization of $(\text{GT})_{15}$ -SWCNTs (300 ms exposure time in NIR) without Lipofectamine Crisprmax and (F) with Lipofectamine Crisprmax (100 ms exposure time in NIR).

Nevertheless, internalized $(\text{GT})_{15}$ -SWCNTs with and without Lipofectamine Crisprmax which were imaged with the same exposure time (Figure 13), where the $(\text{GT})_{15}$ -SWCNTs were visible in the inner surface of the cell, $Z = 4 \mu\text{m}$. There was no evident enhancement of cellular internalization of $(\text{GT})_{15}$ -SWCNTs that were pretreated with Lipofectamine Crisprmax (Figure 13a) (magenta dashed circle) compared to cellular internalization of

(GT)₁₅-SWCNTs that were not pretreated (Figure 13b). Furthermore, since some of the clusters were relatively large and were found in focus on the top surface of the cells' membrane, $Z = 12 \mu\text{m}$ (Figure 13a), and blurry in the inner surface of the cell, $Z = 4 \mu\text{m}$ (cyan dashed circles), it could be presumed that a substantial number of clusters adhered to the outer surface of the cell and were not internalized. These clusters, external to the cell, potentially masked internalized SWCNTs in lower Z -planes, hindering direct quantification of SWCNT uptake. These results are in accordance with previous studies, which demonstrated that (GT)₁₅-SWCNTs could form aggregates by different methods of suspension⁸⁴, and that aggregates and accumulation of (GT)₁₅-SWCNTs may occur within the cell^{83,89}. Given the tendency of the (GT)₁₅-SWCNTs to aggregate, we hypothesize that the cationic lipid bilayer of the Lipofectamine Crisprmax further enhances the clustering of the (GT)₁₅-SWCNTs, possibly due to their negative charge.

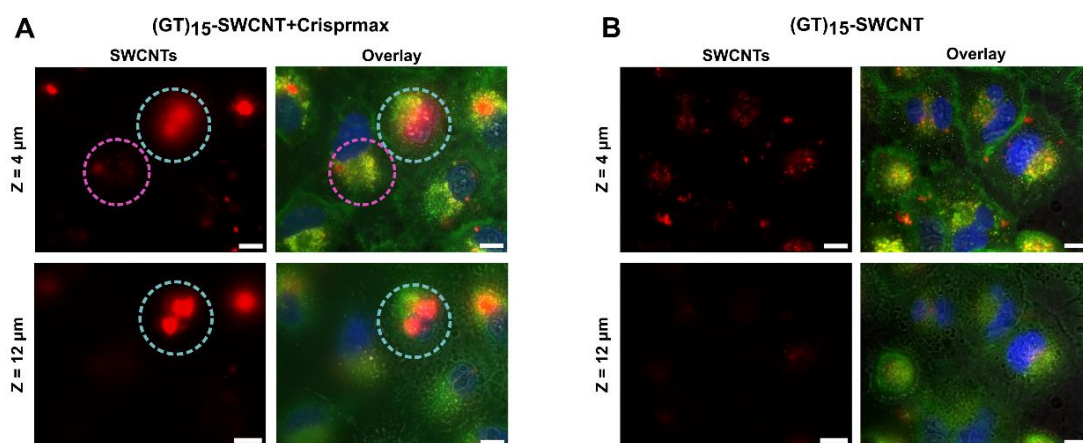


Figure 13. Images of A549 cells following overnight incubation with 0.3 mg L^{-1} (GT)₁₅-SWCNTs (A) pretreated with Lipofectamine Crisprmax and (B) without Lipofectamine Crisprmax, for different Z positions. The images were obtained using a $100\times$ objective. Scale bars for all images are $10 \mu\text{m}$. Top row: $Z = 4 \mu\text{m}$, an inner surface of the cell. Bottom row: $Z = 12 \mu\text{m}$, the top surface of the cell. Left column: the SWCNTs imaged in the NIR fluorescence channel (300 ms exposure time for (A) and (B)). Right column: the overlay of the NIR fluorescence channel of the SWCNTs with the visible fluorescence channel of the cell organelles, which were fluorescently stained with CellMask (green) for the membrane, Hoechst 33258 (blue) for the nuclei, and LysoTracker (yellow) for the lysosome. In (A), the cyan dashed circles mark clusters of (GT)₁₅-SWCNTs that are adhered to the outer top surface of the cell, which appears in focus in the $Z = 12 \mu\text{m}$ surface, where the cell organelles appear blurry. The magenta dashed circle marks single SWCNTs that were internalized in a cell and located in the lysosome area.

To ascertain our working concentration of Lipofectamine Crisprmax, we investigated its impact on cell viability for several concentrations. We started with $0.75 \mu\text{l}$ of

Lipofectamine Crisprmax for a well containing 300 μl samples, in accordance with the manufacturer protocol, and tested the effect of 0.5 \times , 1 \times , 2 \times , and 4 \times , corresponding to 0.375 μl , 0.75 μl , 1.5 μl , and 3 μl Lipofectamine Crisprmax, respectively. A549 cells were incubated overnight with the different quantities of Lipofectamine Crisprmax in an 8 well μ -Slide, and their viability was quantified on the following day by Hoechst and Propidium Iodide (PI) fluorescent dyes staining, which distinguished between the live and dead cells, respectively (Figure 14).

The cell viability was found to be 99%, 96%, 96%, 90%, and 45% for 0 μl , 0.375 μl , 0.75 μl , 1.5 μl , and 3 μl of Lipofectamine Crisprmax, respectively. Furthermore, the number of live cells compared to the control, indicating the proliferation of the cells, was found to be 100%, 93%, 63%, and 21% for 0.375 μl , 0.75 μl , 1.5 μl , and 3 μl of Lipofectamine Crisprmax, respectively.

While 0.375 μl and 0.75 μl of Lipofectamine Crisprmax resulted in similar cell viability, higher quantities decreased the viability.

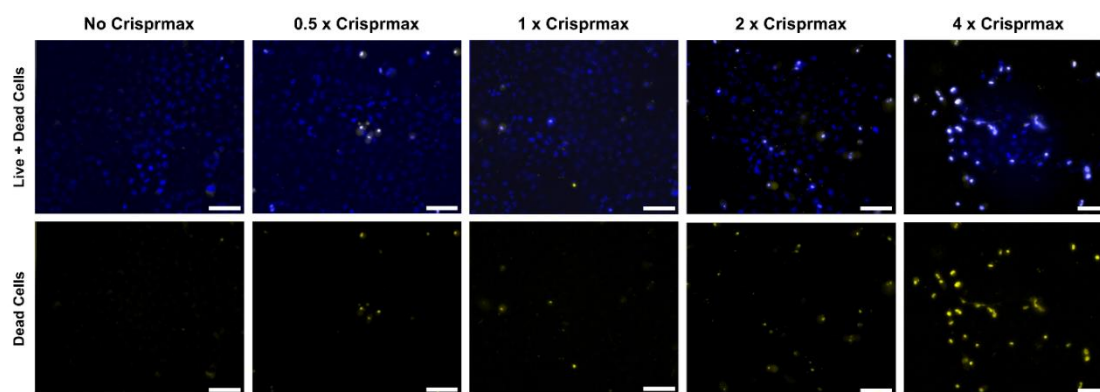


Figure 14. Cell viability of A549 cells following overnight incubation with different quantities of Lipofectamine Crisprmax. The blue indicates the nucleus of live cells, stained with Hoechst, yellow indicates the nucleus of dead cells and fragments of the nucleus as a result of necrosis, stained with Propidium iodide (PI), and light purple is an overlap of both fluorescent dyes indicating cells which underwent apoptosis. The images in the top row are of the live and dead cells, and the images in the bottom row are only dead cells. The columns are the different quantities of Lipofectamine Crisprmax per well from left to right: 0 μl , 0.375 μl , 0.75 μl , 1.5 μl , and 3 μl . The images were obtained using a 20 \times objective. The scale bar for all images is 100 μm .

We further investigated the efficiency of the cellular internalization of the different PEG-SWCNTs for different quantities of Lipofectamine Crisprmax (Figure 15). We pretreated

0.3 mg L⁻¹ PEG-SWCNTs with different quantities of Lipofectamine Crisprmax, 0.375 μ l, 0.75 μ l, 1.5 μ l, and 3 μ l, and incubated them overnight with A549 cells in an 8 well μ -Slide. The representative fluorescent images in the NIR indicate that for higher quantities of Lipofectamine Crisprmax, the cellular uptake was more efficient. Yet, due to the balance between the impact of Lipofectamine Crisprmax on the cell viability and the internalization enhancement of PEG-SWCNTs, we chose to use the quantity of Lipofectamine Crisprmax recommended in the manufacturer protocol.

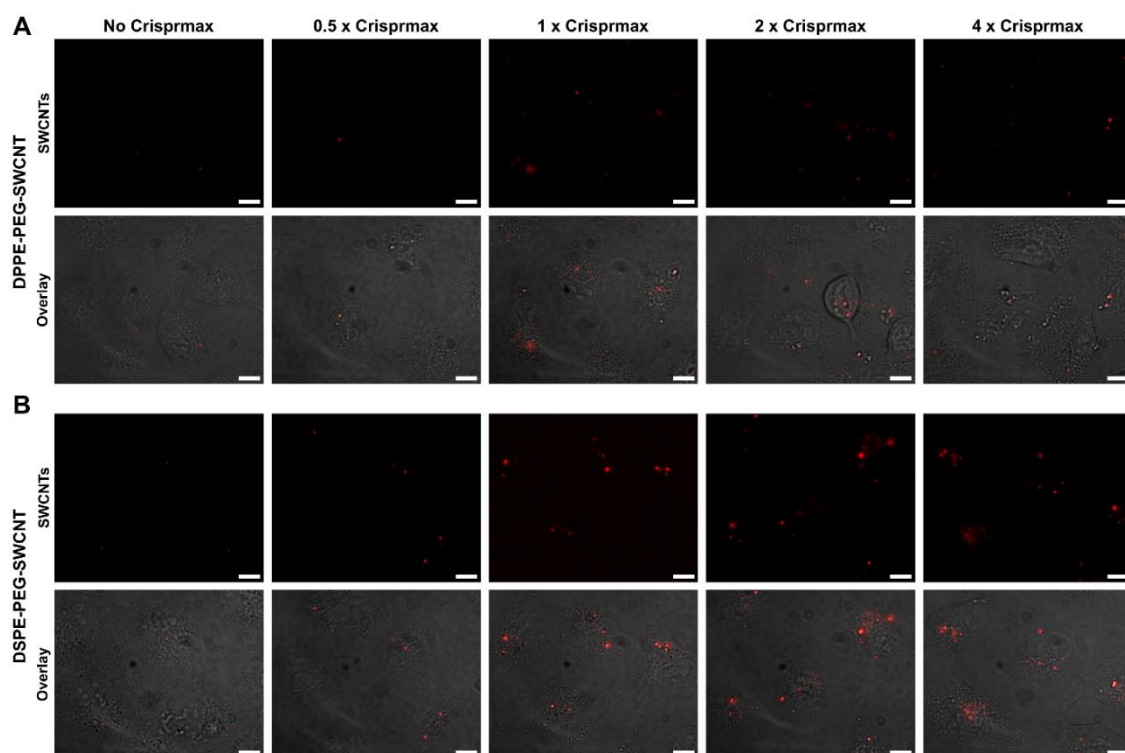


Figure 15. Internalization efficiency of PEG-SWCNTs (0.3 mg L⁻¹) when pretreated with different quantities of Lipofectamine Crisprmax in A549 cells. For (A) DPPE-PEG-SWCNTs and (B) DSPE-PEG-SWCNTs. The images were obtained using a 100 \times objective. Scale bars for all images are 10 μ m. The top row in each panel are the internalized SWCNTs by the cells imaged in the NIR channel (800 ms and 400 ms exposure time for (A) DPPE-PEG-SWCNTs and (B) DSPE-PEG-SWCNTs, respectively), and the bottom row is the overlay of the internalized SWCNTs with the bright field image of the cells. The columns are the different quantities of Lipofectamine Crisprmax per well that were mixed with 0.3 mg L⁻¹ PEG-SWCNTs from left to right: 0 μ l, 0.375 μ l, 0.75 μ l, 1.5 μ l, and 3 μ l.

We then wanted to examine if different quantities of Lipofectamine Crisprmax affected the clustering of (GT)₁₅-SWCNTs, in an attempt to enhance their cellular internalization. We therefore pretreated (GT)₁₅-SWCNTs with three different quantities of Lipofectamine Crisprmax, 0.375 μ l, 0.75 μ l, and 1.5 μ l, and incubated them overnight with A549 cells

in an 8 well μ -Slide (Figure 16). The representative NIR fluorescence images taken the following day showed that (GT)₁₅-SWCNTs formed clusters for all quantities of Lipofectamine Crisprmax, implying the ineffectiveness of using Lipofectamine Crisprmax for enhancing the internalization of (GT)₁₅-SWCNTs.

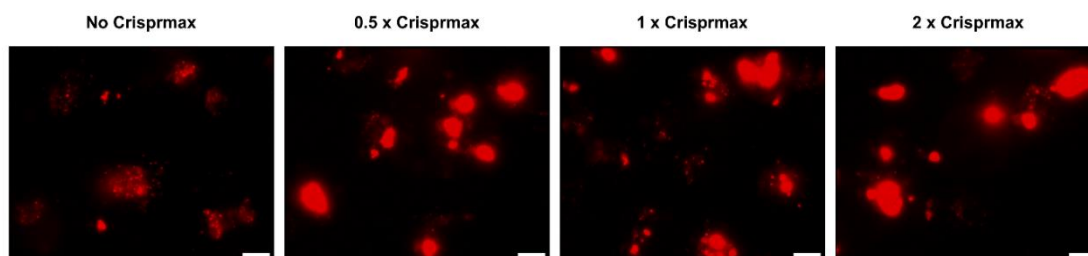


Figure 16. Cluster formation of (GT)₁₅-SWCNTs (0.3 mg L^{-1}) when pretreated with different quantities of Lipofectamine Crisprmax imaged in the NIR fluorescence channel (300 ms exposure time) following overnight incubation with A549 cells. The images were obtained using a $100\times$ objective. Scale bars for all images are $10 \mu\text{m}$. The columns are the different quantities of Lipofectamine Crisprmax that were mixed with 0.3 mg L^{-1} (GT)₁₅-SWCNTs from left to right: $0 \mu\text{l}$, $0.375 \mu\text{l}$, $0.75 \mu\text{l}$, and $1.5 \mu\text{l}$.

The internalization of the different functionalized SWCNTs by HEK293T cells can be observed in the representative images presented in Figure 17. For HEK293T cells, the uptake of DPPE-PEG-SWCNT (Figure 17a) was very scarce and was not enhanced by Lipofectamine Crisprmax (Figure 17b). However, the internalization of DSPE-PEG-SWCNT by HEK293T cells (Figure 17c) was more efficient than the internalization of DPPE-PEG-SWCNT and was further enhanced with Lipofectamine Crisprmax (Figure 17d). Yet, the location of the nanoparticles relative to the organelles of the HEK293T cells was more difficult to determine, due to the more scattered locations of the lysosomes. Similar to the A549 cells, the uptake of the (GT)₁₅-SWCNTs in HEK293T cells was higher than the uptake of the PEGylated functionalized SWCNTs even when pretreated with Lipofectamine Crisprmax (Figure 17e). Moreover, the (GT)₁₅-SWCNTs pretreated with Lipofectamine Crisprmax presented clusters (Figure 17f), which is consistent with our results for the A549 cells (Figure 12f) and the TEM images (Figure 11), showing the formation of (GT)₁₅-SWCNT clusters in the presence of Lipofectamine Crisprmax. These results further support our conclusion that the usage of Lipofectamine

Crisprmax is not advised for cellular internalization of (GT)₁₅-SWCNTs. Moreover, the advantage of SWCNTs pretreated with Lipofectamine Crisprmax for increasing uptake in HEK293T cells was only noticeable for DSPE-PEG-SWCNTs.

Comparing the internalization of the different functionalized SWCNT in A549 cells with HEK293T cells, it is evident that the uptake of SWCNTs by the A549 cancerous cell line was higher than the uptake of SWCNTs by the HEK293T cells. This could be explained by previous findings, which demonstrated an increase of endocytosis pathways in epithelial cancerous cells, leading to a higher uptake of nanoparticles compared to non-cancerous epithelial cells^{135,136}. These findings can encourage future studies on drug delivery systems for cancerous cells utilizing different functionalized SWCNTs.

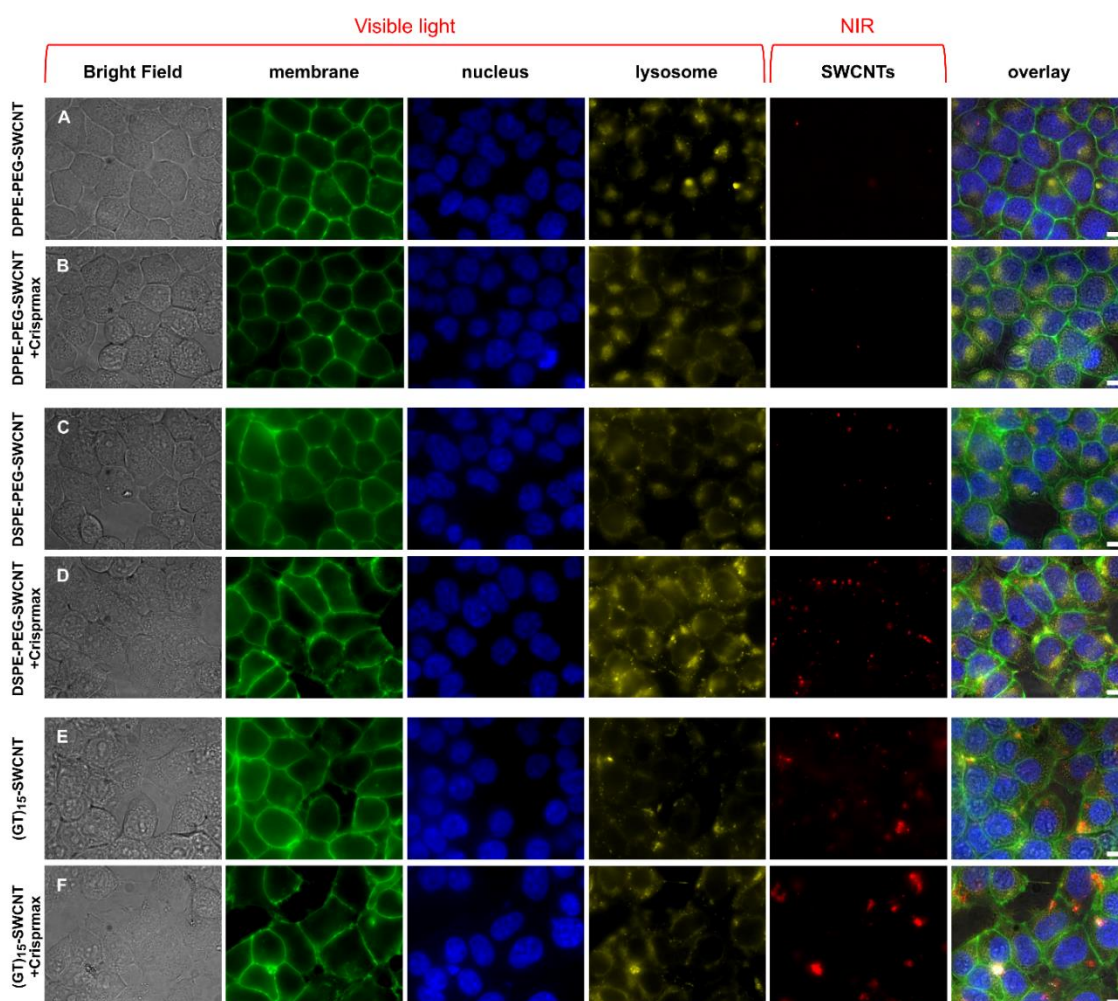


Figure 17. Fluorescence microscopy images of SWCNTs (0.3 mg L^{-1}) with different types of functionalization internalized in HEK293T cells without or with Lipofectamine Crisprmax. The cells were stained with fluorescent dyes: CellMask (green) for the membrane, Hoechst 33258 (blue) for the nuclei, and LysoTracker (yellow) for the lysosome. The red indicates the NIR fluorescence of the internalized SWCNTs within the cells. The columns from left to right: bright field images, the visible fluorescence channels of the membrane, nucleus, lysosomes, the NIR fluorescence channel of the SWCNTs, and the overlay of all the different fluorescence images, in the visible and NIR. The images were obtained using a $100\times$ objective. The scale bars for all the images are $10 \mu\text{m}$. (A) Internalization of DPPE-PEG-SWCNTs (800 ms exposure time in NIR) without Lipofectamine Crisprmax and (B) with Lipofectamine Crisprmax (800 ms exposure time in NIR). (C) Internalization of DSPE-PEG-SWCNTs (800 ms exposure time in NIR) without Lipofectamine Crisprmax and (D) with Lipofectamine Crisprmax (400 ms exposure time in NIR). (E) Internalization of (GT)₁₅-SWCNTs (200 ms exposure time in NIR) without Lipofectamine Crisprmax and (F) with Lipofectamine Crisprmax (50 ms exposure time in NIR).

Z-stack images were taken to better localize the SWCNTs with respect to the cell, and to differentiate between internalized SWCNTs and SWCNTs that adhered to the external surface of the cells. Figure 18 presents representative Z-stack images of the internalization of DSPE-PEG-SWCNTs, which were pretreated with Lipofectamine Crisprmax in A549 cells (Figure 18a) and HEK293T cells (Figure 18b), taken at $2 \mu\text{m}$

spacing in the Z -position, where the bottom surface $z = 0 \mu m$ corresponds to the glass bottom of the well plate, and the top surface was above the focus plane of the upper membrane of the cells. The NIR fluorescence spots that appear in focus in the bottom $z = 0 \mu m$ for both types of cells, could originate from SWCNTs bound to the outer surface of the cells, whereas the internalized SWCNTs appear in focus in Z -positions of the middle planes, in which other cellular organelles are also in focus. The SWCNTs were found to be mostly localized in the lower planes of the cells, in similar locations as that of the lysosomes, further confirming cellular uptake. In the images of the top two Z -slices, on the other hand, there were no SWCNTs that appeared in focus. We, therefore, conclude that DSPE-PEG-SWCNTs did not adhere to the top outer surface of the cell.

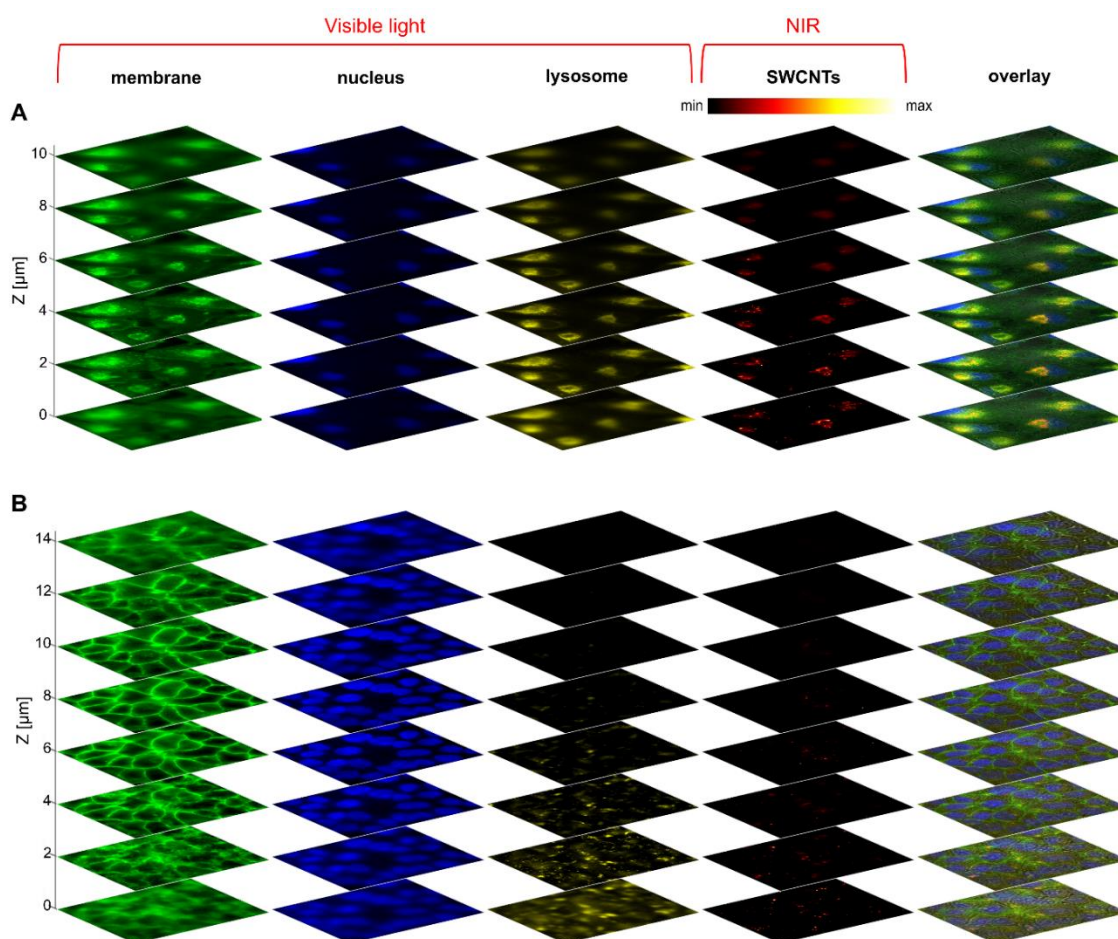


Figure 18. Z-stacks images of the cells following the internalization of 0.3 mg L^{-1} DSPE-PEG-SWCNTs pretreated with Lipofectamine Crisprmax in (A) A549 cells and (B) HEK293T cells. Each image has a field of view (FOV) of $96.6 \mu\text{m} \times 77.2 \mu\text{m}$. The cells were stained with fluorescent dyes: CellMask (green), Hoechst 33258 (blue), and LysoTracker (yellow) for the membrane, nuclei, and lysosome, respectively. The column with the red color (hot color-plate) indicates the NIR fluorescence (400 ms exposure time for (A) and (B)) relative intensity (higher intensity appears yellow) of the internalized SWCNTs within the cells in the different Z heights. The rightmost column is a Z -stack overlay of all the different visible and NIR fluorescence images. In the overlay image, the NIR SWCNT fluorescence appears only in red, to prevent confusion with the yellow label of the lysosomes. The Z -stacks were acquired with a $100\times$ objective and a step size of $2 \mu\text{m}$ between each Z position. The number of steps for each Z -stack was determined by the dimensions of the corresponding cells. The bottom slice, $z = 0 \mu\text{m}$, corresponds to the bottom of the adherent cell on the glass surface. Both the bottom and top slices were captured for heights in which the membranes of the cells were not in focus.

Z -stack images of cells incubated with DPPE-PEG-SWCNTs, which were pretreated with Lipofectamine Crisprmax (Figure 19), presented similar trends of SWCNTs appearing in focus in the Z -positions of the middle planes, mostly in the lower surfaces. In A549 cells, the SWCNTs were mostly colocalized with the lysosomes (Figure 19a), whereas in HEK293T cells, the internalization of the SWCNTs was scarce throughout the different planes (Figure 19b).

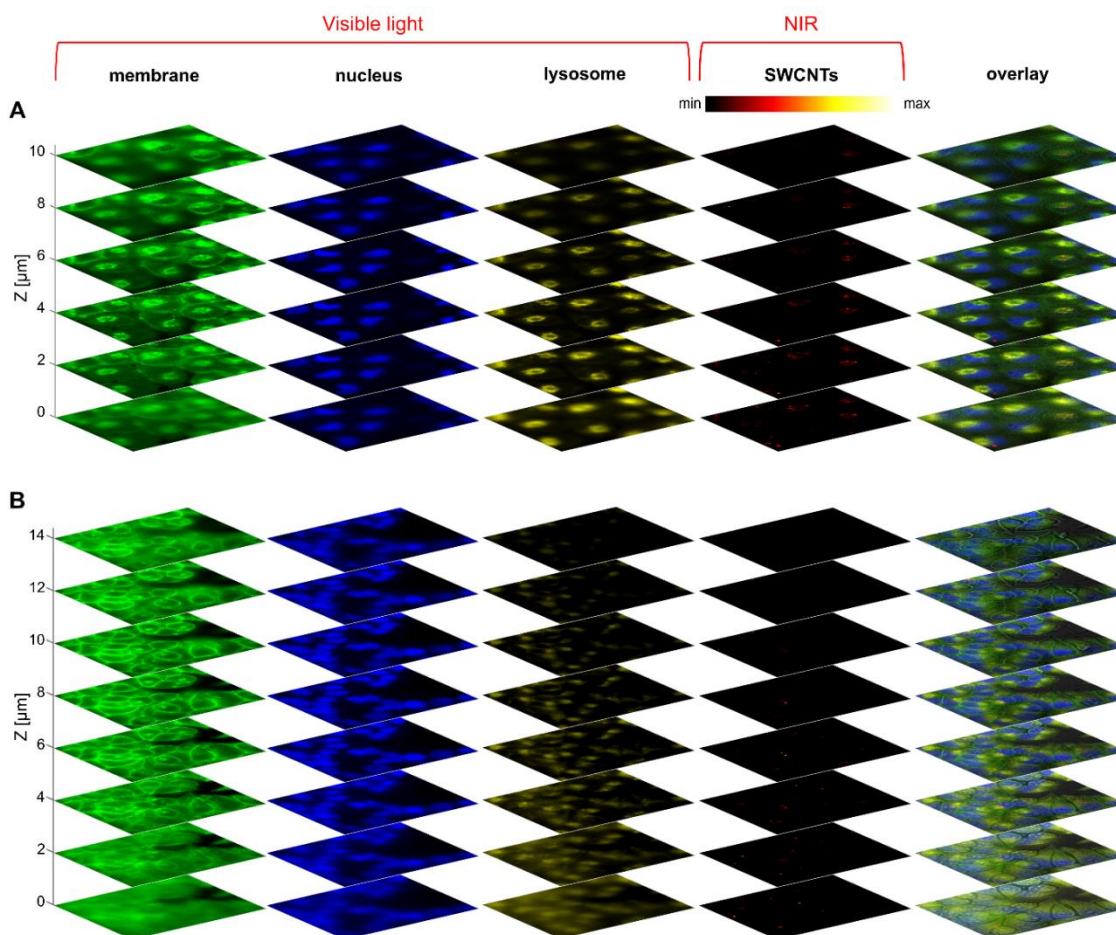


Figure 19. Z-stacks images of the cells following the internalization of 0.3 mg L^{-1} DPPE-PEG-SWCNTs pretreated with Lipofectamine Crisprmax in (A) A549 cells and (B) HEK293T cells. Each image has a field of view (FOV) of $96.6 \mu\text{m} \times 77.2 \mu\text{m}$. The cells were stained with fluorescent dyes: CellMask (green), Hoechst 33258 (blue), and LysoTracker (yellow) for the membrane, nuclei, and lysosome, respectively. The column with the red color (hot color-plate) indicates the NIR fluorescence (800 ms exposure time for (A) and (B)) relative intensity (higher intensity appears yellow) of the internalized SWCNTs within the cells in the different Z heights. The rightmost column is a Z-stack overlay of all the different visible and NIR fluorescence images. In the overlay image, the NIR SWCNT fluorescence appears only in red, to prevent confusion with the yellow label of the lysosomes. The Z-stacks were acquired with a $100\times$ objective and a step size of $2 \mu\text{m}$ between each Z position. The number of steps for each Z-stack was determined by the dimensions of the corresponding cells. The bottom slice, $z = 0 \mu\text{m}$, corresponds to the bottom of the adherent cell on the glass surface. Both the bottom and top slices were captured for heights in which the membranes of the cells were not in focus.

Figure 20 presents representative images of the internalization of $(\text{GT})_{15}$ -SWCNTs in A549 cells (Figure 20a), and HEK293T cells (Figure 20b), taken at $2 \mu\text{m}$ spacing in the Z-position, where the bottom surface $z = 0 \mu\text{m}$ corresponds to the glass bottom of the well plate, and the top surface was just above the focus plane of the upper membrane of

the cells. The NIR fluorescence spots that appear in focus in the bottom slice $z = 0 \mu m$, for both types of cells, correspond to SWCNTs bound to the outer surface of the cells. In contrast, the internalized SWCNTs appear in focus in the Z -positions of the middle planes, in which other cellular organelles are also in focus, whereas SWCNTs bound to the outer surface of the membrane appear blurry in Z planes within the cell (Appendix, Figure A2). The internalized (GT)₁₅-SWCNTs were found to be more distributed across the different planes of the cell, compared to the internalized DSPE-PEG-SWCNTs (Figure 18) and DPPE-PEG-SWCNTs (Figure 19). Yet here too, according to the intensity gradient in the NIR fluorescence channel, most of the SWCNTs were localized in the lower planes of the cells, for both types of cells, colocalized with the lysosomes according to the orange areas in the overlay images.

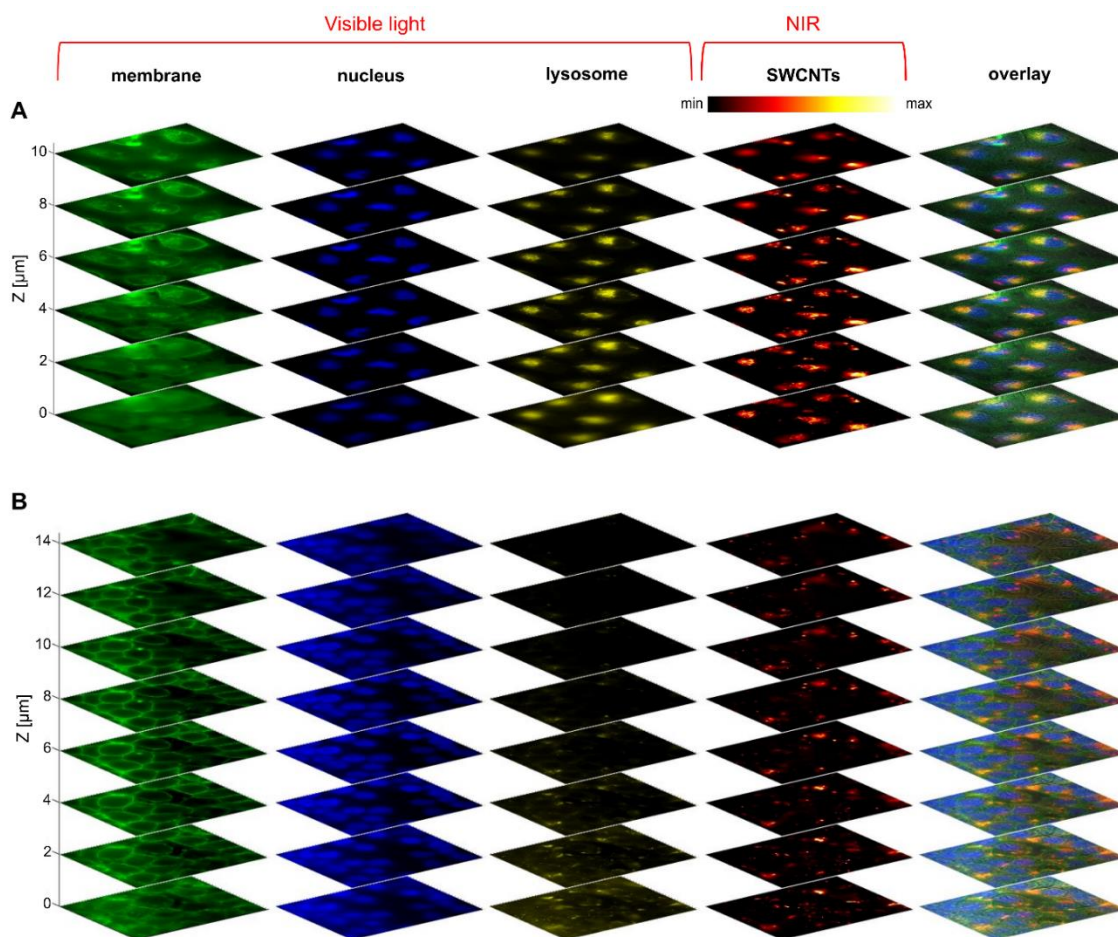


Figure 20. Z-stacks images of the cells following the internalization of 0.3 mg L^{-1} (GT)₁₅-SWCNTs in (A) A549 cells and (B) HEK293T cells. Each image has a field of view (FOV) of $96.6 \mu\text{m} \times 77.2 \mu\text{m}$. The cells were stained with fluorescent dyes: CellMask (green), Hoechst 33258 (blue), and LysoTracker (yellow) for the membrane, nuclei, and lysosome, respectively. The column with the red color (hot color-plate) indicates the NIR fluorescence (300 ms and 200 ms exposure time for (A) and (B) respectively) relative intensity (higher intensity appears yellow) of the internalized SWCNTs within the cells in the different Z heights. The rightmost column is a Z-stack overlay of all the different visible and NIR fluorescence images. In the overlay image, the NIR SWCNT fluorescence appears only in red, to prevent confusion with the yellow label of the lysosomes. The Z-stacks were acquired with a 100 \times objective and a step size of $2 \mu\text{m}$ between each Z position. The number of steps for each Z-stack was determined by the dimensions of the corresponding cells. The bottom slice, $z = 0 \mu\text{m}$, corresponds to the bottom of the adherent cell on the glass surface. Both the bottom and top slices were captured for heights in which the membranes of the cells were not in focus.

3.3 Intracellular fluorescence imaging of internalized functionalized SWCNTs

The efficiency of cellular internalization of the different functionalized SWCNTs was quantified by the NIR fluorescence intensity within each cell, normalized by the cell area, to minimize variance originating from different cell dimensions. To define the perimeters of the cell, we manually segmented the cells into individual regions of interest (ROI) according to the cells' membranes, which were stained with CellMask and captured in the GFP channel of the fluorescence microscope (Figure 21).

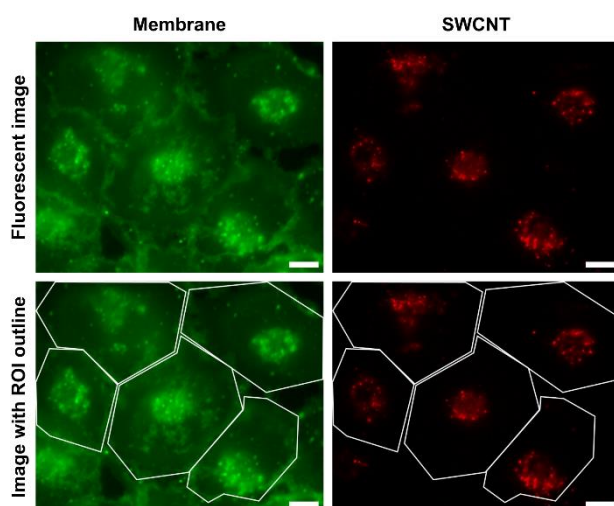


Figure 21. Marked ROI for the analysis of A549 cells following incubation overnight with 0.3 mg L^{-1} DSPE-PEG-SWCNTs pretreated with Lipofectamine Crisprmax. The images were obtained using a $100\times$ objective. Scale bars for all images are $10 \mu\text{m}$. Top row: fluorescence images of the membrane in the visible fluorescence channel (left) and the SWCNTs in the NIR fluorescence channel (right). The bottom row is the overlay of the marked ROI, manually determined by the cell membrane perimeter, with the fluorescence image.

The NIR fluorescence intensity per cell was quantified for two different concentrations of PEG-SWCNTs, 0.15 mg L^{-1} and 0.3 mg L^{-1} . For PEG-SWCNTs, internalization was quantified without or with Lipofectamine Crisprmax, whereas $(\text{GT})_{15}$ -SWCNTs, however, internalization was quantified only without Lipofectamine Crisprmax, since when pretreated with Lipofectamine Crisprmax, they formed large clusters that adhered to the exterior surface of the cell in its presence such that high fluorescence intensity from the external aggregates were observed over several inner Z planes of the cells (Figure 22).

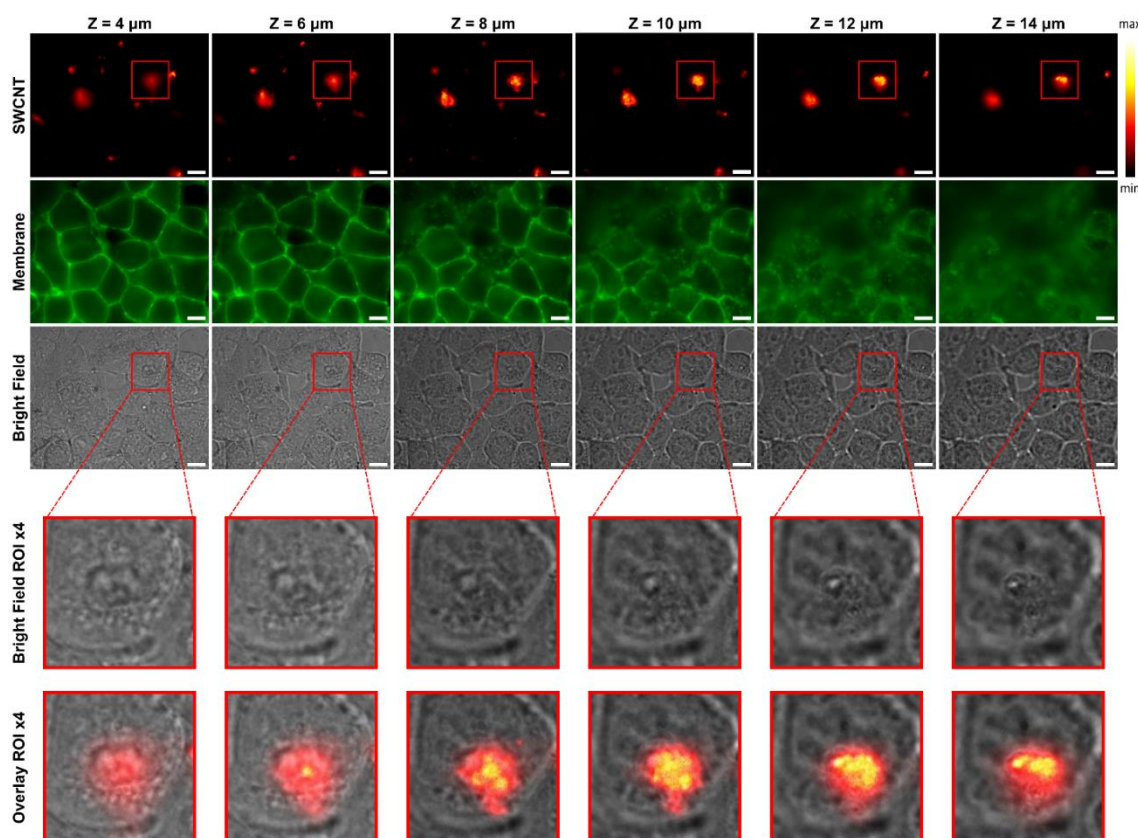


Figure 22. Images of external aggregates observed over several internal surfaces of the cell. HEK293T cells following overnight incubation with 0.3 mg L^{-1} (GT)₁₅-SWCNTs pretreated with Lipofectamine Crisprmax for different Z positions. The images were obtained using a 100× objective. Scale bars for all images are 10 μm. The columns represent 6 different Z positions with increments of 2 μm between adjacent columns, from left to right. The left column is at Z = 4 μm, which is a surface within the cell, and the rightmost column is at z = 14 μm is the top exterior surface of the cells where the membrane appears out of focus. The rows from top to bottom: SWCNTs acquired in the NIR SWCNT fluorescence channel (50 ms exposure time), visible fluorescence images of membranes of cells stained with Cell Mask, bright-field images of the cells, marked ROI in the bright-field imaged enlarged by ×4 and marked ROI of the overlay of the bright-field and the NIR SWCNT fluorescence. The red square (ROI) marks a cluster of SWCNTs which appear in focus in the external surface Z = 14 μm, and is imaged along several internal surfaces of the cell, where the membrane appears in focus. For surface Z = 14 μm in the enlarged ROI in the bright-field image, the cell appears out of focus, whereas the cluster appears in focus in the NIR channel image. When descending in the Z positions, the cell gets in focus, while the cluster loses focus.

Internalizing DPPE-PEG-SWCNTs into A549 cells (Figure 23a), the mean intensity per cell area was roughly 1.5 times higher in the case of SWCNTs pretreated with Lipofectamine Crisprmax compared to SWCNTs alone, for both SWCNTs concentrations. Without Lipofectamine Crisprmax, the intensity of the DPPE-PEG-SWCNTs within the A549 cells was similar for the low and high DPPE-PEG-SWCNTs concentrations, and it also reached a similar value for the Lipofectamine Crisprmax treated samples. However, comparing the mean intensity per cell area for internalized

DSPE-PEG-SWCNTs in the A549 cells, the enhancement is significantly higher in the presence of Lipofectamine Crisprmax. While the DSPE-PEG-SWCNTs intensity is similar without Lipofectamine Crisprmax for both SWCNTs concentrations, it is 5 or 8 times higher for the low and high SWCNT concentrations, respectively, when pretreated with Lipofectamine Crisprmax. These findings suggest that pretreatment of PEG-SWCNTs with Lipofectamine Crisprmax increases the internalization of the SWCNTs into A549 cells, and more so for the negatively charged DSPE-PEG-SWCNTs, manifested by the larger internalization enhancement factor for DSPE-PEG-SWCNTs when pretreated with Lipofectamine Crisprmax compared to DPPE-PEG-SWCNTs pretreated with Lipofectamine Crisprmax. The higher uptake of DSPE-PEG-SWCNTs pretreated with Lipofectamine Crisprmax, could potentially be attributed to more efficient interaction with the cationic lipid bilayer of Lipofectamine Crisprmax, possibly owing to the negative charge of the carboxyl on the DSPE-PEG, in contrast to the neutral DPPE-PEG. The internalization of (GT)₁₅-SWCNTs by A549 cells, on the other hand, is more efficient than the internalization of PEG-SWCNTs, even in the presence of Lipofectamine Crisprmax, and it increases with higher SWCNTs concentration.

Internalizing SWCNTs into HEK293T cells (Figure 23b) shows similar trends as the A549, with different enhancement factors. Here, the mean intensity per cell area was roughly 1.2 times higher in the case of DPPE-PEG-SWCNTs pretreated with Lipofectamine Crisprmax compared to DPPE-PEG-SWCNTs alone, for both SWCNTs concentrations. For the negatively charged DSPE-PEG-SWCNT, the enhancement with Lipofectamine Crisprmax was by a factor of 2 for both SWCNT concentrations, which is an overall higher enhancement compared to the internalization of DPPE-PEG-SWCNTs into HEK293T cells, but lower compared to the enhancement of internalization of DSPE-PEG-SWCNTs into A549 cells, with Lipofectamine Crisprmax. The internalization of (GT)₁₅-SWCNTs into HEK293T cells is also the most efficient compared to the PEG-

SWCNT, even with Lipofectamine Crisprmax, and it significantly increases for the higher (GT)₁₅-SWCNTs concentration, similar to the A549 cells. Although Lipofectamine Crisprmax cannot be used with (GT)₁₅-SWCNTs due to the aggregation effect, increasing the concentration of the (GT)₁₅-SWCNTs, for both cell types, can result in higher uptake.

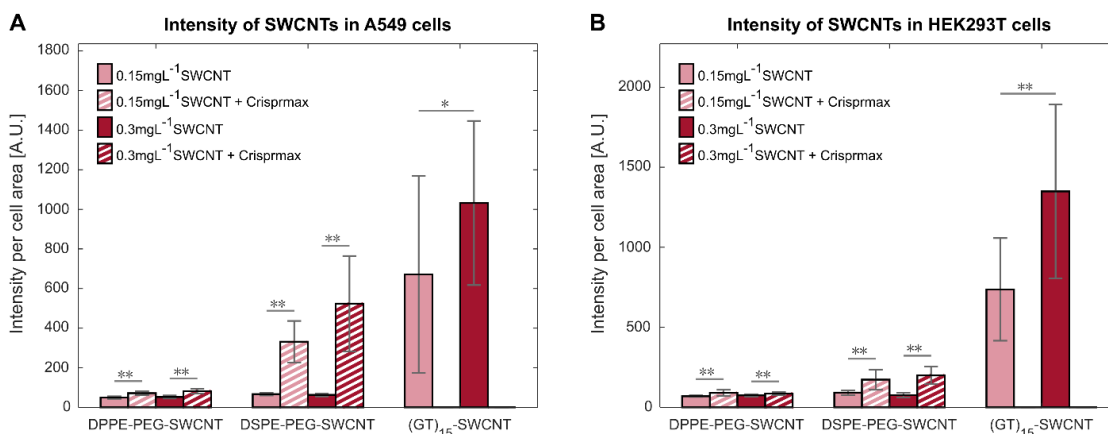


Figure 23. Intracellular NIR fluorescence intensity of DPPE-PEG-SWCNTs, DSPE-PEG-SWCNTs, and (GT)₁₅-SWCNTs (400 ms exposure time) per cell area for two different SWCNTs concentrations within (A) A549 cells ($n \geq 11$ cells per condition) and (B) HEK293T cells ($n \geq 26$ cells per condition). The hatched lines indicate the SWCNTs pretreated with Lipofectamine Crisprmax. The bars represent the average, and the error bars represent the mean \pm standard deviation for each condition. The p values were calculated by a two-sample t-test (** $p < 0.01$ and * $p < 0.05$).

3.4 Colocalization analysis of internalized SWCNTs with the Lysosomes of the cell

To better determine the location of the SWCNTs within the cells, we analyzed the colocalization between the internalized SWCNTs (0.3 mg L⁻¹) and the lysosomes of the cells (Figure 24). We performed the analysis for A549 cells with the PEG-SWCNTs, which were pretreated with Lipofectamine Crisprmax, and with (GT)₁₅-SWCNTs, since the SWCNT fluorescence and the cells' lysosomes appeared to be overlapping (Figure 12b, 12d, and 12e). Figure 24a presents an image of an A549 cell that internalized DSPE-PEG-SWCNTs that were pretreated with Lipofectamine Crisprmax, showing fluorescence channels of the SWCNTs and the lysosomes, and their overlay. The NIR fluorescence of the SWCNTs appears in red, and the fluorescently stained lysosomes appear in yellow. The cell's perimeter was manually marked by a white line to determine

the ROI for analysis. In the overlay of both channels, it is apparent that most internalized SWCNTs overlap with the lysosomes. Figure 24b is the colocalization fluorogram of the cell in Figure 24a, which is essentially a scatterplot of the intensities of both fluorescence channels. The x-axis represents the intensities captured in the NIR SWCNT fluorescence channel, while the y-axis represents the intensities captured in the lysosomes' fluorescence channel. Noticeably, higher intensities of the SWCNTs correlate with the higher intensities from the lysosomes, indicating that the SWCNTs are indeed colocalized with the lysosomes.

The colocalization between the SWCNTs and lysosomes was further quantified by finding the Pearson correlation coefficient and Manders coefficient¹³⁷. Pearson's correlation coefficient (PCC), which is the normalized covariance of two variables, is defined as:

$$PCC = \frac{\sum_i (R_i - \bar{R}) * (Y_i - \bar{Y})}{\sqrt{\sum_i (R_i - \bar{R})^2 * \sum_i (Y_i - \bar{Y})^2}} \quad (4)$$

where R_i and Y_i are the intensities of pixel i for the red and yellow channels respectively, and \bar{R} and \bar{Y} are the mean intensities from the red and yellow channels respectively, where the two channels can represent any dual-channel image. While Pearson's coefficient accounts for correlations and similarity in the positions of the pixels in the two channels, Mander's coefficients are sensitive to the channel's intensity as well, and are defined as^{138,139}:

$$M_1 = \frac{\sum_i R_{i, colocal}}{\sum_i R_i} \quad (5)$$

for $R_{i, colocal} = R_i$ if $Y_i > 0$ and $R_{i, colocal} = 0$ if $Y_i = 0$, and

$$M_2 = \frac{\sum_i Y_{i, colocal}}{\sum_i Y_i} \quad (6)$$

for $Y_{i, colocal} = Y_i$ if $R_i > 0$ and $Y_{i, colocal} = 0$ if $R_i = 0$.

In other words, M_1 is the average intensity of the red (SWCNTs) channel calculated over pixels having non-zero intensity in the yellow (lysosome) channel, and vice versa for M_2 .

Essentially, M_1 is the fraction of SWCNTs encapsulated in the lysosomes, and M_2 is the fraction of lysosomes overlapping with the SWCNTs. In order to eliminate noise from the calculations of Manders coefficients, a threshold is determined, such that only pixels with intensities higher than the threshold are calculated in equations (5) and (6). We used the Otsu auto-threshold to prevent bias in the results.

The colocalization coefficients of the SWCNTs with the lysosomes for PEG-SWCNTs pretreated with Lipofectamine Crisprmax and (GT)₁₅-SWCNTs alone are described in Figure 24c. The Pearson correlation coefficients for the DPPE-PEG-SWCNT, DSPE-PEG-SWCNT, and the (GT)₁₅-SWCNTs were 0.59, 0.76, and 0.85, respectively, indicating the positive correlation resulting from the colocalization between the SWCNT and the lysosomes. The M_1 Manders overlap coefficients for the DPPE-PEG-SWCNT, DSPE-PEG-SWCNT, and the (GT)₁₅-SWCNTs were 0.85, 0.94 and 0.94, respectively, indicating that most of the SWCNTs were colocalized with the lysosomes, where the fraction of colocalized SWCNTs was higher for the DSPE-PEG-SWCNT and (GT)₁₅-SWCNT. The M_2 Manders overlap coefficients for the DPPE-PEG-SWCNT, DSPE-PEG-SWCNT, and the (GT)₁₅-SWCNTs, which indicate the area fraction of the lysosomes that overlap with SWCNTs, were 0.43, 0.58, and 0.74, respectively. The internalization quantification analysis showed that the cellular uptake of DSPE-PEG-SWCNTs pretreated with Lipofectamine Crisprmax was higher than the uptake of DPPE-PEG-SWCNTs pretreated with Lipofectamine Crisprmax, and the cellular uptake of (GT)₁₅-SWCNT was higher than both PEG-SWCNTs pretreated with Lipofectamine Crisprmax. Given that the majority of internalized SWCNTs is indeed localized within the lysosomes, manifested in the high values of M_1 , we expect that increased uptake would correlate with higher values of M_2 owing to a larger area of the lysosomes that overlap with the SWCNTs, supported by the different $\frac{M_2}{M_1}$ ratios for the different types of SWCNTs. The results of the colocalization analysis further confirm that the SWCNTs

entered the cells via endocytosis, as the vast majority of the SWCNTs were located in the lysosomes.

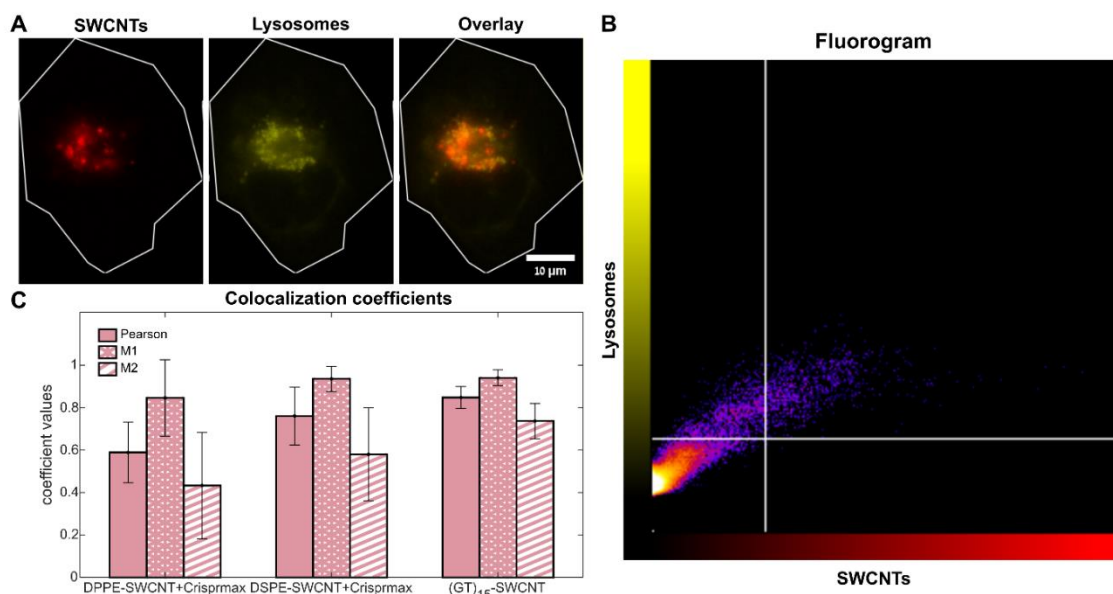


Figure 24. Colocalization analysis of the SWCNTs with lysosomes in A549 cells for PEG-SWCNTs pretreated with Lipofectamine Crisprmax and (GT)₁₅-SWCNTs. (A) An A549 cell which internalized DSPE-PEG-SWCNTs that were pretreated with Lipofectamine Crisprmax. From left to right: NIR fluorescence channel of the internalized SWCNTs, lysosomes stained with LysoTracker channel, and the overlay of the NIR SWCNT fluorescence and the lysosomes channels. The white line indicates the perimeter of the cell. (B) A scatter plot of the intensities from the NIR SWCNT fluorescence channel against the intensities from the lysosome channel of the cell in (A). (C) Colocalization coefficients for DPPE-PEG-SWCNTs and DSPE-PEG-SWCNTs pretreated with Lipofectamine Crisprmax and (GT)₁₅-SWCNTs alone ($n \geq 15$ cells per type of SWCNT): Pearson’s correlation coefficient (full bar), Manders coefficients M_1 (star pattern), and M_2 (hatched pattern). The bars represent the average, and the error bars represent the standard deviation.

The colocalization analysis of the different internalized SWCNTs (0.3 mg L^{-1}) with the lysosomes of HEK293T cell showed that over 50% of the SWCNTs overlapped with the lysosome (Figure 25). The Pearson correlation coefficients for the DPPE-PEG-SWCNT, DSPE-PEG-SWCNT, and the (GT)₁₅-SWCNTs were 0.1, 0.24, and 0.21, respectively. The relatively low Pearson coefficients can be attributed to the more scattered locations of the lysosomes, and the relatively low uptake of the SWCNTs by the HEK293T cells (Figure 17) compared to the uptake of the SWCNTs by the A549 cells (Figure 12). The M_1 Manders overlap coefficients for the DPPE-PEG-SWCNT, DSPE-PEG-SWCNT, and the (GT)₁₅-SWCNTs were 0.78, 0.65 and 0.53, respectively, indicating that most of the SWCNTs were colocalized with the lysosomes, indicating that the main pathway of

internalization was via endocytosis. The M_2 Manders overlap coefficients for the DPPE-PEG-SWCNT, DSPE-PEG-SWCNT, and the (GT)₁₅-SWCNTs, which indicate the area fraction of the lysosomes that overlap with SWCNTs, were 0.02, 0.13, and 0.11, respectively. The internalization of DPPE-PEG-SWCNTs pretreated with Lipofectamine Crisprmax by the HEK293T cells was relatively low (Figure 17), such for a single Z position, only 1 or 2 fluorescent spots were observed. This could explain the relatively high M_1 coefficient and the low M_2 coefficient, since most of the SWCNTs were observed in the lysosomes of the cells, but not many were indeed internalized. Consequently, most of the lysosome area did not overlap with SWCNTs. Compared to the internalization of the different SWCNTs by the A549 cells, the colocalization of the SWCNTs with the lysosomes was lower for the HEK293T cells. Still, the analysis suggests that most of the SWCNTs entered the HEK293T cells via endocytosis.

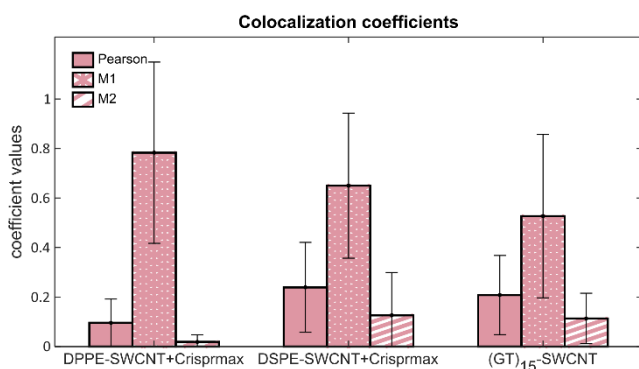


Figure 25. Colocalization analysis of the internalized functionalized SWCNTs with the lysosomes of HEK293T cells. The graph presents Pearson’s correlation coefficient (full bar), Manders coefficients M_1 (star pattern), and M_2 (hatched pattern), for DPPE-PEG-SWCNTs and DSPE-PEG-SWCNTs pretreated with Lipofectamine Crisprmax, and (GT)₁₅-SWCNTs without Lipofectamine Crisprmax ($n \geq 17$ cells per type of SWCNT). The bars represent the average, and the error bars represent the standard deviation.

3.5 Cell viability

The cells continued to proliferate following incubation with the different functionalized SWCNTs overnight, with and without Lipofectamine Crisprmax, and appeared viable the following day. To further assess the cell viability, we stained the cells with Hoechst and Propidium Iodide (PI) fluorescent dyes to distinguish between the live and dead cells,

respectively (Figure 26). Hoechst is a cell membrane permeable DNA dye which, upon binding to the adenine-thymine (A-T) in the minor groove, emits bright blue fluorescence in live cells. This occurs when the DNA is in a condensed state, therefore, Hoechst can stain apoptotic cells where the chromatin is in a highly condensed form¹⁴⁰, leading to a higher dye uptake and brighter fluorescence from apoptotic cells compared to live cells¹⁴¹. PI stain, on the other hand, binds to the nucleus of cells with ruptured membranes, associated with late-stage apoptosis and necrosis. Importantly, PI cannot stain viable cells owing to their intact membrane¹⁴¹. In the cell viability analysis image, the live cells appear blue, the necrotic cells yellow, and the apoptotic cells exhibit bright fluorescence from both channels, resulting in a purple color¹⁴². Our analysis indicated that the cell viability was high without adverse cytotoxicity. These findings align with prior work that demonstrated minimal cytotoxic effects when using low concentrations of functionalized SWCNTs^{143,144}. Furthermore, in previous research, Lipofectamine Crisprmax presented high cell viability for various cell types, including A549 cells and HEK293 cells⁹⁹.

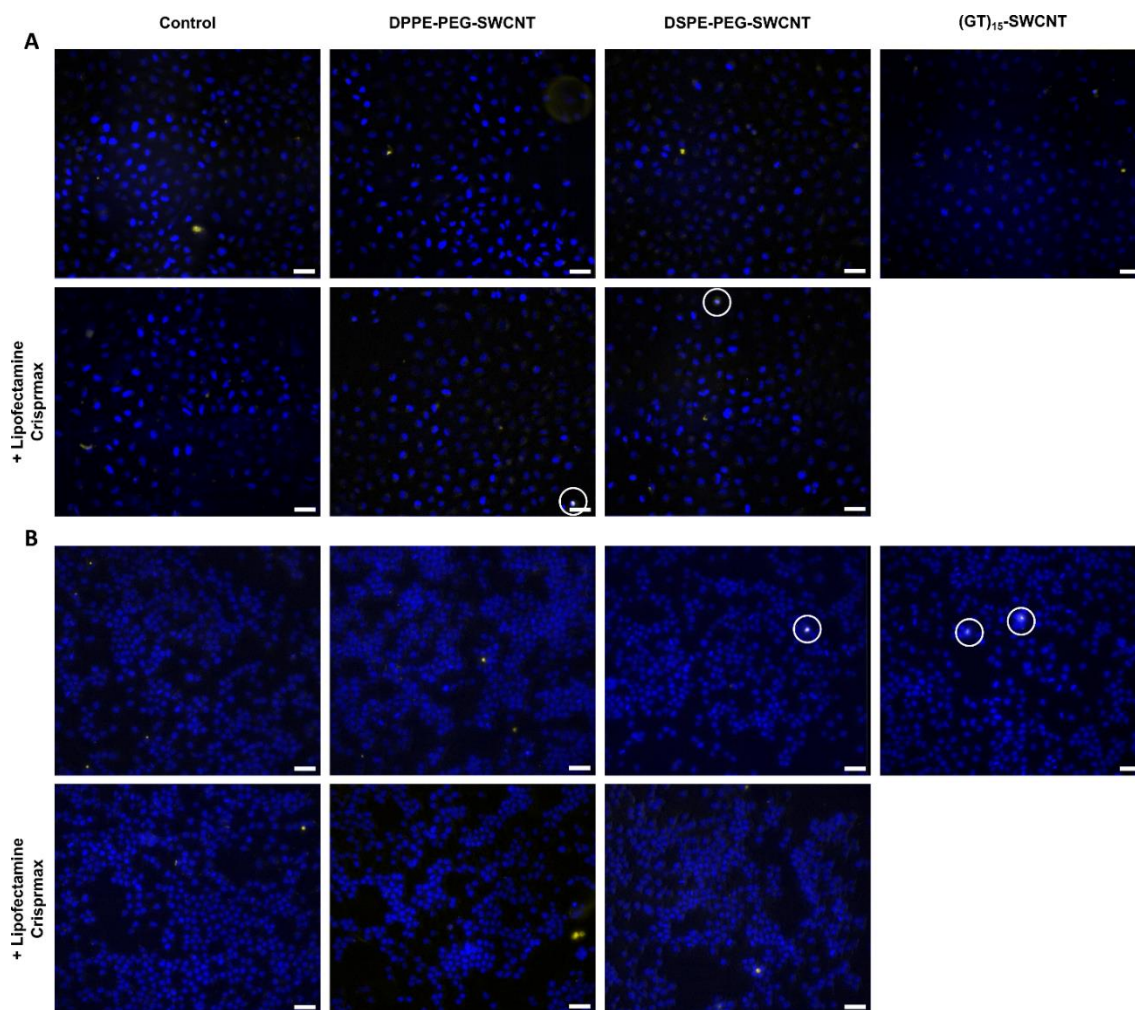


Figure 26. Images demonstrating cell viability following overnight incubation with different types of functionalized SWCNTs (0.3 mg L^{-1}) for cell types (a) A549 and (b) HEK293T. The blue indicates the nucleus of lives cells, stained with Hoechst, yellow indicates the nucleus of dead cells and fragments of the nucleus as a result of necrosis, stained with Propidium iodide (PI), and light purple, marked with a circle, is an overlap of both fluorescent dyes indicating cells which underwent apoptosis. The column from left to right: control, DPPE-PEG-SWCNT, DSPE-PEG-SWCNT, and $(\text{GT})_{15}$ -SWCNT, where for the bottom row, the SWCNTs were pretreated with Lipofectamine Crisprmax. The images were obtained using a $20\times$ objective. The scale bar for all images is $50 \mu\text{m}$.

4 Conclusions

We have demonstrated a novel approach for enhancing cellular internalization of PEGylated functionalized SWCNTs using Lipofectamine Crisprmax. Notably, the internalization of the negatively charged DSPE-PEG-SWCNT with Lipofectamine Crisprmax was more efficient compared to the internalization of the neutral DPPE-PEG-SWCNT with Lipofectamine Crisprmax. Furthermore, we showed that utilizing Lipofectamine Crisprmax to enhance cellular internalization of PEGylated functionalized SWCNTs was more efficient compared to the strategy of increasing the SWCNTs concentration alone. Comparing the internalization of the different PEGylated functionalized SWCNTs, pretreated with Lipofectamine Crisprmax, in A549 cells versus HEK293T cells, the SWCNTs uptake by the A549 cancerous cell line was higher than the SWCNTs uptake by the HEK293T cells. These findings could be explained by previous research that showed an increased endocytosis uptake of nanoparticles in epithelial cancerous cells, whereas in non-cancerous epithelial cells, endocytosis was limited^{135,136}.

In the attempt to enhance cellular internalization of ssDNA functionalized SWCNTs, namely (GT)₁₅-SWCNTs, with Lipofectamine Crisprmax, the SWCNTs formed large clusters of various sizes, resulting in poorer optical performances. Some of the clusters that were too large to enter the cell adhered to its external surface. The fluorescence emission of such large clusters, although situated outside the cell, was also detectable in focal planes within the cell, impairing our ability to identify unambiguously fluorescence spots that truly originated from internalized SWCNTs. We, therefore, concluded that utilizing Lipofectamine Crisprmax is not a preferred method for enhancing cellular internalization of ssDNA functionalized SWCNT, (GT)₁₅-SWCNT. Nevertheless, increasing the concentration of (GT)₁₅-SWCNTs increased the SWCNT uptake by the cells.

Our colocalization analysis showed that the vast majority of the internalized SWCNTs were localized within the lysosomes, and even more so for A549 cells, which further confirmed that the SWCNTs predominantly entered the cells via endocytosis. Furthermore, we confirmed high cell viability for the SWCNT concentrations used in our study.

These findings serve as a potential catalyst for future studies focusing on bio-sensing and bio-imaging utilizing functionalized SWCNTs that would otherwise exhibit limited cellular internalization in the absence of Lipofectamine Crisprmax. Additionally, owing to the biocompatibility and the ability to overcome the cellular membrane barrier, the utilization of different functionalized SWCNTs pretreated with Lipofectamine Crisprmax could be explored *in vivo* to elucidate their potential as a versatile nanoparticle-based drug delivery carrier¹⁴⁵ targeting the lysosome in malignant cells. Further investigations will delve into the effects of Lipofectamine Crisprmax or other transfection reagents on diverse types of functionalized SWCNTs or other nanoparticles and their internalization across various cell types, as well as the optimization of the internalization strategy for specific applications.

References

- (1) Harish, V.; Tewari, D.; Gaur, M.; Yadav, A. B.; Swaroop, S.; Bechelany, M.; Barhoum, A. Review on Nanoparticles and Nanostructured Materials: Bioimaging, Biosensing, Drug Delivery, Tissue Engineering, Antimicrobial, and Agro-Food Applications. *Nanomaterials*. 2022. <https://doi.org/10.3390/nano12030457>.
- (2) Joudeh, N.; Linke, D. Nanoparticle Classification, Physicochemical Properties, Characterization, and Applications: A Comprehensive Review for Biologists. *Journal of Nanobiotechnology*. 2022. <https://doi.org/10.1186/s12951-022-01477-8>.
- (3) Khan, I.; Saeed, K.; Khan, I. Nanoparticles: Properties, Applications and Toxicities. *Arabian Journal of Chemistry*. 2019. <https://doi.org/10.1016/j.arabjc.2017.05.011>.
- (4) Cooper, G. Structure of the Plasma Membrane. In *The Cell: A Molecular Approach*.; Sinauer Associates: Sunderland (MA), 2000.
- (5) Donahue, N. D.; Acar, H.; Wilhelm, S. Concepts of Nanoparticle Cellular Uptake, Intracellular Trafficking, and Kinetics in Nanomedicine. *Advanced Drug Delivery Reviews*. 2019. <https://doi.org/10.1016/j.addr.2019.04.008>.
- (6) Behzadi, S.; Serpooshan, V.; Tao, W.; Hamaly, M. A.; Alkawareek, M. Y.; Dreaden, E. C.; Brown, D.; Alkilany, A. M.; Farokhzad, O. C.; Mahmoudi, M. Cellular Uptake of Nanoparticles: Journey inside the Cell. *Chemical Society Reviews*. 2017. <https://doi.org/10.1039/c6cs00636a>.
- (7) Vardharajula, S.; Ali, S. Z.; Tiwari, P. M.; Eroğlu, E.; Vig, K.; Dennis, V. A.; Singh, S. R. Functionalized Carbon Nanotubes: Biomedical Applications. *International Journal of Nanomedicine*. 2012. <https://doi.org/10.2147/IJN.S35832>.
- (8) Bastings, M. M. C.; Anastassacos, F. M.; Ponnuswamy, N.; Leifer, F. G.; Cuneo,

- G.; Lin, C.; Ingber, D. E.; Ryu, J. H.; Shih, W. M. Modulation of the Cellular Uptake of DNA Origami through Control over Mass and Shape. *Nano Lett.* **2018**. <https://doi.org/10.1021/acs.nanolett.8b00660>.
- (9) Rajwar, A.; Shetty, S. R.; Vaswani, P.; Morya, V.; Barai, A.; Sen, S.; Sonawane, M.; Bhatia, D. Geometry of a DNA Nanostructure Influences Its Endocytosis: Cellular Study on 2D, 3D, and in Vivo Systems. *ACS Nano* **2022**. <https://doi.org/10.1021/acsnano.2c01382>.
- (10) Augustine, R.; Hasan, A.; Primavera, R.; Wilson, R. J.; Thakor, A. S.; Kevadiya, B. D. Cellular Uptake and Retention of Nanoparticles: Insights on Particle Properties and Interaction with Cellular Components. *Materials Today Communications*. 2020. <https://doi.org/10.1016/j.mtcomm.2020.101692>.
- (11) Bettinger, H. F. Carbon Nanotubes: Basic Concepts and Physical Properties. By S. Reich, C. Thomsen, J. Maultzsch. *ChemPhysChem* **2004**. <https://doi.org/10.1002/cphc.200400387>.
- (12) Kruss, S.; Hilmer, A. J.; Zhang, J.; Reuel, N. F.; Mu, B.; Strano, M. S. Carbon Nanotubes as Optical Biomedical Sensors. *Advanced Drug Delivery Reviews*. 2013. <https://doi.org/10.1016/j.addr.2013.07.015>.
- (13) Bachilo, S. M.; Strano, M. S.; Kittrell, C.; Hauge, R. H.; Smalley, R. E.; Weisman, R. B. Structure-Assigned Optical Spectra of Single-Walled Carbon Nanotubes. *Science (80-.)*. **2002**. <https://doi.org/10.1126/science.1078727>.
- (14) Ackermann, J.; Metternich, J. T.; Herbertz, S.; Kruss, S. Biosensing with Fluorescent Carbon Nanotubes. *Angewandte Chemie - International Edition*. 2022. <https://doi.org/10.1002/anie.202112372>.
- (15) Weisman, R. B.; Bachilo, S. M. Dependence of Optical Transition Energies on Structure for Single-Walled Carbon Nanotubes in Aqueous Suspension: An Empirical Kataura Plot. *Nano Lett.* **2003**. <https://doi.org/10.1021/nl034428i>.

- (16) Qiu, L.; Ding, F. Understanding Single-Walled Carbon Nanotube Growth for Chirality Controllable Synthesis. *Accounts Mater. Res.* **2021**. <https://doi.org/10.1021/accountsmr.1c00111>.
- (17) Irita, M.; Yamamoto, T.; Homma, Y. Chirality Distributions for Semiconducting Single-Walled Carbon Nanotubes Determined by Photoluminescence Spectroscopy. *Nanomaterials* **2021**. <https://doi.org/10.3390/nano11092309>.
- (18) Bonis-O'Donnell, J. T. D.; Page, R. H.; Beyene, A. G.; Tindall, E. G.; McFarlane, I. R.; Landry, M. P. Dual Near-Infrared Two-Photon Microscopy for Deep-Tissue Dopamine Nanosensor Imaging. *Adv. Funct. Mater.* **2017**. <https://doi.org/10.1002/adfm.201702112>.
- (19) Iverson, N. M.; Barone, P. W.; Shandell, M.; Trudel, L. J.; Sen, S.; Sen, F.; Ivanov, V.; Atolia, E.; Farias, E.; McNicholas, T. P.; Reuel, N.; Parry, N. M. A.; Wogan, G. N.; Strano, M. S. In Vivo Biosensing via Tissue-Localizable near-Infrared-Fluorescent Single-Walled Carbon Nanotubes. *Nat. Nanotechnol.* **2013**. <https://doi.org/10.1038/nnano.2013.222>.
- (20) Hendler-Neumark, A.; Wulf, V.; Bisker, G. In Vivo Imaging of Fluorescent Single-Walled Carbon Nanotubes within *C. Elegans* Nematodes in the near-Infrared Window. *Mater. Today Bio* **2021**. <https://doi.org/10.1016/j.mtbio.2021.100175>.
- (21) Iverson, N. M.; Bisker, G.; Farias, E.; Ivanov, V.; Ahn, J.; Wogan, G. N.; Strano, M. S. Quantitative Tissue Spectroscopy of near Infrared Fluorescent Nanosensor Implants. *J. Biomed. Nanotechnol.* **2016**. <https://doi.org/10.1166/jbn.2016.2237>.
- (22) Nandi, S.; Caicedo, K.; Cognet, L. When Super-Resolution Localization Microscopy Meets Carbon Nanotubes. *Nanomaterials*. **2022**. <https://doi.org/10.3390/nano12091433>.
- (23) Boghossian, A. A.; Zhang, J.; Barone, P. W.; Reuel, N. F.; Kim, J. H.; Heller, D.

- A.; Ahn, J. H.; Hilmer, A. J.; Rwei, A.; Arkalgud, J. R.; Zhang, C. T.; Strano, M. S. Near-Infrared Fluorescent Sensors Based on Single-Walled Carbon Nanotubes for Life Sciences Applications. *ChemSusChem*. 2011. <https://doi.org/10.1002/cssc.201100070>.
- (24) Bisker, G.; Dong, J.; Park, H. D.; Iverson, N. M.; Ahn, J.; Nelson, J. T.; Landry, M. P.; Kruss, S.; Strano, M. S. Protein-Targeted Corona Phase Molecular Recognition. *Nat. Commun.* **2016**. <https://doi.org/10.1038/ncomms10241>.
- (25) Hendler-Neumark, A.; Bisker, G. Fluorescent Single-Walled Carbon Nanotubes for Protein Detection. *Sensors (Switzerland)*. 2019. <https://doi.org/10.3390/s19245403>.
- (26) Galassi, T. V.; Antman-Passig, M.; Yaari, Z.; Jessurun, J.; Schwartz, R. E.; Heller, D. A. Long-Term in Vivo Biocompatibility of Single-Walled Carbon Nanotubes. *PLoS One* **2020**. <https://doi.org/10.1371/journal.pone.0226791>.
- (27) Tan, J. M.; Arulselvan, P.; Fakurazi, S.; Ithnin, H.; Hussein, M. Z. A Review on Characterizations and Biocompatibility of Functionalized Carbon Nanotubes in Drug Delivery Design. *Journal of Nanomaterials*. 2014. <https://doi.org/10.1155/2014/917024>.
- (28) Pan, J.; Li, F.; Choi, J. H. Single-Walled Carbon Nanotubes as Optical Probes for Bio-Sensing and Imaging. *J. Mater. Chem. B* **2017**. <https://doi.org/10.1039/c7tb00748e>.
- (29) Jena, P. V.; Roxbury, D.; Galassi, T. V.; Akkari, L.; Horoszko, C. P.; Iaea, D. B.; Budhathoki-Uprety, J.; Pipalia, N.; Haka, A. S.; Harvey, J. D.; Mittal, J.; Maxfield, F. R.; Joyce, J. A.; Heller, D. A. A Carbon Nanotube Optical Reporter Maps Endolysosomal Lipid Flux. *ACS Nano* **2017**. <https://doi.org/10.1021/acsnano.7b04743>.
- (30) Antonucci, A.; Reggente, M.; Gillen, A. J.; Roullier, C.; Lambert, B. P.;

- Boghossian, A. A. Differential Near-Infrared Imaging of Heterocysts Using Single-Walled Carbon Nanotubes. *Photochem. Photobiol. Sci.* **2023**. <https://doi.org/10.1007/s43630-022-00302-3>.
- (31) Ehrlich, R.; Wulf, V.; Hendler-Neumark, A.; Kagan, B.; Bisker, G. Super-Resolution Radial Fluctuations (SRRF) Nanoscopy in the near Infrared. *Opt. Express* **2022**. <https://doi.org/10.1364/oe.440441>.
- (32) Kagan, B.; Hendler-Neumark, A.; Wulf, V.; Kamber, D.; Ehrlich, R.; Bisker, G. Super-Resolution Near-Infrared Fluorescence Microscopy of Single-Walled Carbon Nanotubes Using Deep Learning. *Adv. Photonics Res.* **2022**. <https://doi.org/10.1002/adpr.202200244>.
- (33) Sharaga, E.; Hendler-Neumark, A.; Kamber, D.; Bisker, G. Spatiotemporal Tracking of Near-Infrared Fluorescent Single-Walled Carbon Nanotubes in *C. Elegans* Nematodes Confined in a Microfluidics Platform. *Adv. Mater. Technol.* **2023**, *2301222*, 1–17. <https://doi.org/10.1002/admt.202301222>.
- (34) Boonyaves, K.; Ang, M. C. Y.; Park, M.; Cui, J.; Khong, D. T.; Singh, G. P.; Koman, V. B.; Gong, X.; Porter, T. K.; Choi, S. W.; Chung, K.; Chua, N. H.; Urano, D.; Strano, M. S. Near-Infrared Fluorescent Carbon Nanotube Sensors for the Plant Hormone Family Gibberellins. *Nano Lett.* **2023**. <https://doi.org/10.1021/acs.nanolett.2c04128>.
- (35) Sultana, N.; Dewey, H.; Budhathoki-Uprety, J. Optical Detection of PH Changes in Artificial Sweat Using Near-Infrared Fluorescent Nanomaterials. *Sensors & Diagnostics* **2022**. <https://doi.org/10.1039/d2sd00110a>.
- (36) Amir, D.; Hendler-Neumark, A.; Wulf, V.; Ehrlich, R.; Bisker, G. Oncometabolite Fingerprinting Using Fluorescent Single-Walled Carbon Nanotubes. *Adv. Mater. Interfaces* **2022**. <https://doi.org/10.1002/admi.202101591>.
- (37) Loewenthal, D.; Kamber, D.; Bisker, G. Monitoring the Activity and Inhibition of

- Cholinesterase Enzymes Using Single-Walled Carbon Nanotube Fluorescent Sensors. *Anal. Chem.* **2022**. <https://doi.org/10.1021/acs.analchem.2c02471>.
- (38) Wulf, V.; Bichachi, E.; Hendler-Neumark, A.; Massarano, T.; Leshem, A. B.; Lampel, A.; Bisker, G. Multicomponent System of Single-Walled Carbon Nanotubes Functionalized with a Melanin-Inspired Material for Optical Detection and Scavenging of Metals. *Adv. Funct. Mater.* **2022**. <https://doi.org/10.1002/adfm.202209688>.
- (39) Gaikwad, P.; Rahman, N.; Parikh, R.; Crespo, J.; Cohen, Z.; Williams, R. Optical Nanosensor Passivation Enables Highly Sensitive Detection of the Inflammatory Cytokine IL-6. **2023**.
- (40) Kuo, M.; Raffaele, J. F.; Waller, E. M.; Varaljay, V. A.; Wagner, D.; Kelley-loughnane, N.; Reuel, N. F. Screening Enzymatic Degradation of Polyester Polyurethane with Fluorescent Single-Walled Carbon Nanotube and Polymer Nanoparticle Conjugates. **2023**. <https://doi.org/10.1021/acsnano.3c04347>.
- (41) Hendler-Neumark, A.; Wulf, V.; Bisker, G. Single-Walled Carbon Nanotube Sensor Selection for the Detection of MicroRNA Biomarkers for Acute Myocardial Infarction as a Case Study. *ACS Sensors* **2023**. <https://doi.org/10.1021/acssensors.3c00633>.
- (42) Yoon, M.; Lee, Y.; Lee, S.; Cho, Y.; Koh, D.; Shin, S.; Tian, C.; Song, Y.; Kang, J.; Cho, S. A NIR Fluorescent Single Walled Carbon Nanotube Sensor for Broad-Spectrum Diagnostics. *Sensors & Diagnostics* **2024**. <https://doi.org/10.1039/d3sd00257h>.
- (43) Ehrlich, R.; Hendler-Neumark, A.; Wulf, V.; Amir, D.; Bisker, G. Optical Nanosensors for Real-Time Feedback on Insulin Secretion by β -Cells. *Small* **2021**. <https://doi.org/10.1002/sml.202101660>.
- (44) Bisker, G.; Bakh, N. A.; Lee, M. A.; Ahn, J.; Park, M.; O'Connell, E. B.; Iverson,

- N. M.; Strano, M. S. Insulin Detection Using a Corona Phase Molecular Recognition Site on Single-Walled Carbon Nanotubes. *ACS Sensors* **2018**. <https://doi.org/10.1021/acssensors.7b00788>.
- (45) Gerstman, E.; Hendler-neumark, A.; Wulf, V.; Bisker, G. Monitoring the Formation of Fibrin Clots as Part of the Coagulation Cascade Using Fluorescent Single-Walled Carbon Nanotubes. *ACS Appl. Mater. Interfaces* **2023**. <https://doi.org/10.1021/acscami.3c00828>.
- (46) Hofferber, E.; Meier, J.; Herrera, N.; Stapleton, J.; Calkins, C.; Iverson, N. Detection of Single Walled Carbon Nanotube Based Sensors in a Large Mammal. *Nanomedicine Nanotechnology, Biol. Med.* **2022**. <https://doi.org/10.1016/j.nano.2021.102489>.
- (47) Ackermann, J.; Stegemann, J.; Smola, T.; Reger, E.; Jung, S.; Schmitz, A.; Herbertz, S.; Erpenbeck, L.; Seidl, K.; Kruss, S. High Sensitivity Near-Infrared Imaging of Fluorescent Nanosensors. *Small* **2023**. <https://doi.org/10.1002/smll.202206856>.
- (48) Nißler, R.; Ackermann, J.; Ma, C.; Kruss, S. Prospects of Fluorescent Single-Chirality Carbon Nanotube-Based Biosensors. *Analytical Chemistry*. 2022. <https://doi.org/10.1021/acs.analchem.2c01321>.
- (49) Kelich, P.; Jeong, S.; Navarro, N.; Adams, J.; Sun, X.; Zhao, H.; Landry, M. P.; Vuković, L. Discovery of DNA-Carbon Nanotube Sensors for Serotonin with Machine Learning and Near-Infrared Fluorescence Spectroscopy. *ACS Nano* **2022**. <https://doi.org/10.1021/acsnano.1c08271>.
- (50) Kallmyer, N. E.; Musielewicz, J.; Sutter, J.; Reuel, N. F. Substrate-Wrapped, Single-Walled Carbon Nanotube Probes for Hydrolytic Enzyme Characterization. *Anal. Chem.* **2018**. <https://doi.org/10.1021/acs.analchem.7b05444>.
- (51) Shao, W.; Paul, A.; Zhao, B.; Lee, C.; Rodes, L.; Prakash, S. Carbon Nanotube

- Lipid Drug Approach for Targeted Delivery of a Chemotherapy Drug in a Human Breast Cancer Xenograft Animal Model. *Biomaterials* **2013**. <https://doi.org/10.1016/j.biomaterials.2013.09.007>.
- (52) Karchemski, F.; Zucker, D.; Barenholz, Y.; Regev, O. Carbon Nanotubes-Liposomes Conjugate as a Platform for Drug Delivery into Cells. *J. Control. Release* **2012**. <https://doi.org/10.1016/j.jconrel.2011.12.037>.
- (53) Yazdani, S.; Mozaffarian, M.; Pazuki, G.; Hadidi, N.; Gallego, I.; Puras, G.; Pedraz, J. L. Design of Double Functionalized Carbon Nanotube for Amphotericin B and Genetic Material Delivery. *Sci. Rep.* **2022**. <https://doi.org/10.1038/s41598-022-25222-1>.
- (54) Antonucci, A.; Kupis-Rozmysłowicz, J.; Boghossian, A. A. Noncovalent Protein and Peptide Functionalization of Single-Walled Carbon Nanotubes for Biodelivery and Optical Sensing Applications. *ACS Applied Materials and Interfaces*. 2017. <https://doi.org/10.1021/acsami.7b00810>.
- (55) Rosenberg, D. J.; Cunningham, F. J.; Hubbard, J. D.; Goh, N. S.; Wang, J. W.-T.; Nishitani, S.; Hayman, E. B.; Hura, G. L.; Landry, M. P.; Pinals, R. L. Mapping the Morphology of DNA on Carbon Nanotubes in Solution Using X-Ray Scattering Interferometry. *J. Am. Chem. Soc.* **2023**. <https://doi.org/10.1021/jacs.3c09549>.
- (56) Johnson, R. R.; Johnson, A. T. C.; Klein, M. L. Probing the Structure of DNA-Carbon Nanotube Hybrids with Molecular Dynamics. *Nano Lett.* **2008**. <https://doi.org/10.1021/nl071909j>.
- (57) Alizadehmojarad, A. A.; Bachilo, S. M.; Weisman, R. B. Compositional Analysis of SsDNA-Coated Single-Wall Carbon Nanotubes through UV Absorption Spectroscopy. *Nano Lett.* **2022**. <https://doi.org/10.1021/acs.nanolett.2c02850>.
- (58) Lei, K.; Bachilo, S. M.; Weisman, R. B. Kinetics of Single-Wall Carbon Nanotube

- Coating Displacement by Single-Stranded DNA Depends on Nanotube Structure. *ACS Nano* **2023**. <https://doi.org/10.1021/acsnano.3c06906>.
- (59) Zhang, J.; Landry, M. P.; Barone, P. W.; Kim, J. H.; Lin, S.; Ulissi, Z. W.; Lin, D.; Mu, B.; Boghossian, A. A.; Hilmer, A. J.; Rwei, A.; Hinckley, A. C.; Kruss, S.; Shandell, M. A.; Nair, N.; Blake, S.; Şen, F.; Şen, S.; Croy, R. G.; Li, D.; Yum, K.; Ahn, J. H.; Jin, H.; Heller, D. A.; Essigmann, J. M.; Blankschtein, D.; Strano, M. S. Molecular Recognition Using Corona Phase Complexes Made of Synthetic Polymers Adsorbed on Carbon Nanotubes. *Nat. Nanotechnol.* **2013**. <https://doi.org/10.1038/nnano.2013.236>.
- (60) Zhou, Y.; Fang, Y.; Ramasamy, R. P. Non-Covalent Functionalization of Carbon Nanotubes for Electrochemical Biosensor Development. *Sensors (Switzerland)*. 2019. <https://doi.org/10.3390/s19020392>.
- (61) Wulf, V.; Pui-yan Hung, A.; Hendler-Neumark, A.; Li, W.; Shamis, O.; Gozin, M.; Huang, X.; Kin Tak Lau, A.; Bisker, G. Acoustic Performance of Epoxy-Based Composites Incorporating Fluorescent Single-Walled Carbon Nanotubes. *Compos. Part A Appl. Sci. Manuf.* **2023**. <https://doi.org/10.1016/j.compositesa.2023.107667>.
- (62) Neves, L. F. F.; Tsai, T. W.; Palwai, N. R.; Martyn, D. E.; Tan, Y.; Schmidtke, D. W.; Resasco, D. E.; Harrison, R. G. Non-Covalent Attachment of Proteins to Single-Walled Carbon Nanotubes. *Methods Mol. Biol.* **2010**. https://doi.org/10.1007/978-1-60761-579-8_1.
- (63) Wang, S.; Humphreys, E. S.; Chung, S. Y.; Delduco, D. F.; Lustig, S. R.; Wang, H.; Parker, K. N.; Rizzo, N. W.; Subramoney, S.; Chiang, Y. M.; Jagota, A. Peptides with Selective Affinity for Carbon Nanotubes. *Nat. Mater.* **2003**. <https://doi.org/10.1038/nmat833>.
- (64) Shumeiko, V.; Zaken, Y.; Hidas, G.; Paltiel, Y.; Bisker, G.; Shoseyov, O. Peptide-

- Encapsulated Single-Wall Carbon Nanotube-Based Near-Infrared Optical Nose for Bacteria Detection and Classification. *IEEE Sens. J.* **2022**.
<https://doi.org/10.1109/JSEN.2022.3152622>.
- (65) Wulf, V.; Bisker, G. Single-Walled Carbon Nanotubes as Fluorescent Probes for Monitoring the Self-Assembly and Morphology of Peptide/Polymer Hybrid Hydrogels. *Nano Lett.* **2022**. <https://doi.org/10.1021/acs.nanolett.2c01587>.
- (66) Shumeiko, V.; Paltiel, Y.; Bisker, G.; Hayouka, Z.; Shoseyov, O. A Nanoscale Paper-Based near-Infrared Optical Nose (NIRON). *Biosens. Bioelectron.* **2021**.
<https://doi.org/10.1016/j.bios.2020.112763>.
- (67) Mann, F. A.; Horlebein, J.; Meyer, N. F.; Meyer, D.; Thomas, F.; Kruss, S. Carbon Nanotubes Encapsulated in Coiled-Coil Peptide Barrels. *Chem. - A Eur. J.* **2018**.
<https://doi.org/10.1002/chem.201800993>.
- (68) Chio, L.; Del Bonis-O'Donnell, J. T.; Kline, M. A.; Kim, J. H.; McFarlane, I. R.; Zuckermann, R. N.; Landry, M. P. Electrostatic Assemblies of Single-Walled Carbon Nanotubes and Sequence-Tunable Peptoid Polymers Detect a Lectin Protein and Its Target Sugars. *Nano Lett.* **2019**.
<https://doi.org/10.1021/acs.nanolett.8b04955>.
- (69) Wulf, V.; Slor, G.; Rathee, P.; Amir, R. J.; Bisker, G. Dendron-Polymer Hybrids as Tailorable Responsive Coronae of Single-Walled Carbon Nanotubes. *ACS Nano* **2021**. <https://doi.org/10.1021/acsnano.1c09125>.
- (70) Lee, M. A.; Wang, S.; Jin, X.; Bakh, N. A.; Nguyen, F. T.; Dong, J.; Silmore, K. S.; Gong, X.; Pham, C.; Jones, K. K.; Muthupalani, S.; Bisker, G.; Son, M.; Strano, M. S. Implantable Nanosensors for Human Steroid Hormone Sensing In Vivo Using a Self-Templating Corona Phase Molecular Recognition. *Adv. Healthc. Mater.* **2020**. <https://doi.org/10.1002/adhm.202000429>.
- (71) Budhathoki-Uprety, J.; Jena, P. V.; Roxbury, D.; Heller, D. A. Helical

- Polycarbodiimide Cloaking of Carbon Nanotubes Enables Inter-Nanotube Exciton Energy Transfer Modulation. *J. Am. Chem. Soc.* **2014**.
<https://doi.org/10.1021/ja505529n>.
- (72) Farrera, C.; Torres Andón, F.; Feliu, N. Carbon Nanotubes as Optical Sensors in Biomedicine. *ACS Nano*. 2017. <https://doi.org/10.1021/acsnano.7b06701>.
- (73) Kruss, S.; Landry, M. P.; Vander Ende, E.; Lima, B. M. A.; Reuel, N. F.; Zhang, J.; Nelson, J.; Mu, B.; Hilmer, A.; Strano, M. Neurotransmitter Detection Using Corona Phase Molecular Recognition on Fluorescent Single-Walled Carbon Nanotube Sensors. *J. Am. Chem. Soc.* **2014**, *136* (2), 713–724.
<https://doi.org/10.1021/ja410433b>.
- (74) Landry, M. P.; Kruss, S.; Nelson, J. T.; Bisker, G.; Iverson, N. M.; Reuel, N. F.; Strano, M. S. Experimental Tools to Study Molecular Recognition within the Nanoparticle Corona. *Sensors (Switzerland)* **2014**.
<https://doi.org/10.3390/s140916196>.
- (75) Gravely, M.; Safaei, M. M.; Roxbury, D. Biomolecular Functionalization of a Nanomaterial to Control Stability and Retention within Live Cells. *Nano Lett.* **2019**. <https://doi.org/10.1021/acs.nanolett.9b02267>.
- (76) Kallmyer, N. E.; Agarwal, S.; Eeg, D.; Khor, R.; Roby, N.; Vela Ramirez, A.; Hillier, A. C.; Reuel, N. F. Lipid-Functionalized Single-Walled Carbon Nanotubes as Probes for Screening Cell Wall Disruptors. *ACS Appl. Mater. Interfaces* **2023**.
<https://doi.org/10.1021/acsami.3c06592>.
- (77) Antman-Passig, M.; Wong, E.; Frost, G. R.; Cupo, C.; Shah, J.; Agustinus, A.; Chen, Z.; Mancinelli, C.; Kamel, M.; Li, T.; Jonas, L. A.; Li, Y. M.; Heller, D. A. Optical Nanosensor for Intracellular and Intracranial Detection of Amyloid-Beta. *ACS Nano* **2022**. <https://doi.org/10.1021/acsnano.2c00054>.
- (78) Kim, M.; Chen, C.; Yaari, Z.; Frederiksen, R.; Randall, E.; Wollowitz, J.; Cupo,

- C.; Wu, X.; Shah, J.; Worroll, D.; Lagenbacher, R. E.; Goerzen, D.; Li, Y. M.; An, H.; Wang, Y. H.; Heller, D. A. Nanosensor-Based Monitoring of Autophagy-Associated Lysosomal Acidification in Vivo. *Nat. Chem. Biol.* **2023**. <https://doi.org/10.1038/s41589-023-01364-9>.
- (79) Holt, B. D.; Dahl, K. N.; Islam, M. F. Cells Take up and Recover from Protein-Stabilized Single-Wall Carbon Nanotubes with Two Distinct Rates. *ACS Nano* **2012**. <https://doi.org/10.1021/nn300504x>.
- (80) Langenbacher, R.; Budhathoki-Uprety, J.; Jena, P. V.; Roxbury, D.; Streit, J.; Zheng, M.; Heller, D. A. Single-Chirality Near-Infrared Carbon Nanotube Sub-Cellular Imaging and FRET Probes. *Nano Lett.* **2021**. <https://doi.org/10.1021/acs.nanolett.1c01093>.
- (81) Roxbury, D.; Jena, P. V.; Williams, R. M.; Enyedi, B.; Niethammer, P.; Marcet, S.; Verhaegen, M.; Blais-Ouellette, S.; Heller, D. A. Hyperspectral Microscopy of Near-Infrared Fluorescence Enables 17-Chirality Carbon Nanotube Imaging. *Sci. Rep.* **2015**. <https://doi.org/10.1038/srep14167>.
- (82) Jena, P. V.; Gravely, M.; Cupo, C.; Safaei, M. M.; Roxbury, D.; Heller, D. A. Hyperspectral Counting of Multiplexed Nanoparticle Emitters in Single Cells and Organelles. *ACS Nano* **2022**. <https://doi.org/10.1021/acsnano.1c10708>.
- (83) Gravely, M.; Roxbury, D. Multispectral Fingerprinting Resolves Dynamics of Nanomaterial Trafficking in Primary Endothelial Cells. *ACS Nano* **2021**. <https://doi.org/10.1021/acsnano.1c04500>.
- (84) Gravely, M.; Kindopp, A.; Hubert, L.; Card, M.; Nadeem, A.; Miller, C.; Roxbury, D. Aggregation Reduces Subcellular Localization and Cytotoxicity of Single-Walled Carbon Nanotubes. *ACS Appl. Mater. Interfaces* **2022**. <https://doi.org/10.1021/acsnano.1c04500>.
- (85) Galassi, T. V.; Jena, P. V.; Shah, J.; Ao, G.; Molitor, E.; Bram, Y.; Frankel, A.;

- Park, J.; Jessurun, J.; Ory, D. S.; Haimovitz-Friedman, A.; Roxbury, D.; Mittal, J.; Zheng, M.; Schwartz, R. E.; Heller, D. A. An Optical Nanoreporter of Endolysosomal Lipid Accumulation Reveals Enduring Effects of Diet on Hepatic Macrophages in Vivo. *Sci. Transl. Med.* **2018**. <https://doi.org/10.1126/scitranslmed.aar2680>.
- (86) Madani, S. Z. M.; Safaee, M. M.; Gravely, M.; Silva, C.; Kennedy, S.; Bothun, G. D.; Roxbury, D. Carbon Nanotube-Liposome Complexes in Hydrogels for Controlled Drug Delivery via Near-Infrared Laser Stimulation. *ACS Appl. Nano Mater.* **2021**. <https://doi.org/10.1021/acsanm.0c02700>.
- (87) Nadeem, A.; Kindopp, A.; Wyllie, I.; Hubert, L.; Joubert, J.; Lucente, S.; Randall, E.; Jena, P. V.; Roxbury, D. Enhancing Intracellular Optical Performance and Stability of Engineered Nanomaterials via Aqueous Two-Phase Purification. *ACS Nano Lett.* **2023**. <https://doi.org/10.1021/acs.nanolett.3c01727>.
- (88) Yaron, P. N.; Holt, B. D.; Short, P. A.; Lösche, M.; Islam, M. F.; Dahl, K. N. Single Wall Carbon Nanotubes Enter Cells by Endocytosis and Not Membrane Penetration. *J. Nanobiotechnology* **2011**. <https://doi.org/10.1186/1477-3155-9-45>.
- (89) Jin, H.; Heller, D. A.; Strano, M. S. Single-Particle Tracking of Endocytosis and Exocytosis of Single-Walled Carbon Nanotubes in NIH-3T3 Cells. *Nano Lett.* **2008**. <https://doi.org/10.1021/nl072969s>.
- (90) Kam, N. W. S.; Liu, Z.; Dai, H. Carbon Nanotubes as Intracellular Transporters for Proteins and DNA: An Investigation of the Uptake Mechanism and Pathway. *Angew. Chemie - Int. Ed.* **2006**. <https://doi.org/10.1002/anie.200503389>.
- (91) Bhattacharya, S.; Roxbury, D.; Gong, X.; Mukhopadhyay, D.; Jagota, A. DNA Conjugated SWCNTs Enter Endothelial Cells via Rac1 Mediated Macropinocytosis. *Nano Lett.* **2012**. <https://doi.org/10.1021/nl204058u>.
- (92) Kostarelos, K.; Lacerda, L.; Pastorin, G.; Wu, W.; Wieckowski, S.; Luangsivilay,

- J.; Godefroy, S.; Pantarotto, D.; Briand, J. P.; Muller, S.; Prato, M.; Bianco, A. Cellular Uptake of Functionalized Carbon Nanotubes Is Independent of Functional Group and Cell Type. *Nat. Nanotechnol.* **2007**. <https://doi.org/10.1038/nnano.2006.209>.
- (93) Jin, H.; Heller, D. A.; Sharma, R.; Strano, M. S. Size-Dependent Cellular Uptake and Expulsion of Single-Walled Carbon Nanotubes: Single Particle Tracking and a Generic Uptake Model for Nanoparticles. *ACS Nano* **2009**. <https://doi.org/10.1021/nn800532m>.
- (94) Cui, X.; Wan, B.; Yang, Y.; Ren, X.; Guo, L. H. Length Effects on the Dynamic Process of Cellular Uptake and Exocytosis of Single-Walled Carbon Nanotubes in Murine Macrophage Cells /631/80 /704/172 /82/29 /14/19 /14/34 /123 Article. *Sci. Rep.* **2017**. <https://doi.org/10.1038/s41598-017-01746-9>.
- (95) Chong, Z. X.; Yeap, S. K.; Ho, W. Y. Transfection Types, Methods and Strategies: A Technical Review. *PeerJ*. 2021. <https://doi.org/10.7717/peerj.11165>.
- (96) Fus-Kujawa, A.; Prus, P.; Bajdak-Rusinek, K.; Teper, P.; Gawron, K.; Kowalczyk, A.; Sieron, A. L. An Overview of Methods and Tools for Transfection of Eukaryotic Cells in Vitro. *Frontiers in Bioengineering and Biotechnology*. 2021. <https://doi.org/10.3389/fbioe.2021.701031>.
- (97) Cardarelli, F.; Digiacomio, L.; Marchini, C.; Amici, A.; Salomone, F.; Fiume, G.; Rossetta, A.; Gratton, E.; Pozzi, D.; Caracciolo, G. The Intracellular Trafficking Mechanism of Lipofectamine-Based Transfection Reagents and Its Implication for Gene Delivery. *Sci. Rep.* **2016**. <https://doi.org/10.1038/srep25879>.
- (98) Karapurkar, J. K.; Antao, A. M.; Kim, K. S.; Ramakrishna, S. CRISPR-Cas9 Based Genome Editing for Defective Gene Correction in Humans and Other Mammals. In *Progress in Molecular Biology and Translational Science*; 2021. <https://doi.org/10.1016/bs.pmbts.2021.01.018>.

- (99) Yu, X.; Liang, X.; Xie, H.; Kumar, S.; Ravinder, N.; Potter, J.; de Mollerat du Jeu, X.; Chesnut, J. D. Improved Delivery of Cas9 Protein/GRNA Complexes Using Lipofectamine CRISPRMAX. *Biotechnol. Lett.* **2016**. <https://doi.org/10.1007/s10529-016-2064-9>.
- (100) Felgner, P. L.; Gadek, T. R.; Holm, M.; Roman, R.; Chan, H. W.; Wenz, M.; Northrop, J. P.; Ringold, G. M.; Danielsen, M. Lipofection: A Highly Efficient, Lipid-Mediated DNA-Transfection Procedure. *Proc. Natl. Acad. Sci. U. S. A.* **1987**. <https://doi.org/10.1073/pnas.84.21.7413>.
- (101) Zhou, X.; Huang, L. DNA Transfection Mediated by Cationic Liposomes Containing Lipopolylysine: Characterization and Mechanism of Action. *BBA - Biomembr.* **1994**. [https://doi.org/10.1016/0005-2736\(94\)90066-3](https://doi.org/10.1016/0005-2736(94)90066-3).
- (102) Han, P.; Hanlon, D.; Sobolev, O.; Chaudhury, R.; Edelson, R. L. Ex Vivo Dendritic Cell Generation—A Critical Comparison of Current Approaches. In *International Review of Cell and Molecular Biology*; 2019. <https://doi.org/10.1016/bs.ircmb.2019.10.003>.
- (103) Wang, J.; Teng, Z.; Tian, Y.; Fang, T.; Ma, J.; Sun, J.; Zhu, F.; Wu, J.; Wang, X.; Yang, N.; Zhou, X.; Yun, S.; Lu, G. Increasing Cellular Uptake of Mesoporous Silica Nanoparticles in Human Embryonic Kidney Cell Line 293T Cells by Using Lipofectamine 2000. *J. Biomed. Nanotechnol.* **2013**. <https://doi.org/10.1166/jbn.2013.1691>.
- (104) Jalli, R.; Mehrabani, D.; Zare, S.; Saeedi Moghadam, M.; Jamhiri, I.; Manafi, N.; Mehrabani, G.; Ghabanchi, J.; Razeghian Jahromi, I.; Rasouli-Nia, A.; Karimi-Busheri, F. Cell Proliferation, Viability, Differentiation, and Apoptosis of Iron Oxide Labeled Stem Cells Transfected with Lipofectamine Assessed by MRI. *J. Clin. Med.* **2023**, *12* (6). <https://doi.org/10.3390/jcm12062395>.
- (105) Sezgin-Bayindir, Z.; Elcin, A. E.; Parmaksiz, M.; Elcin, Y. M.; Yuksel, N.

- Investigations on Clonazepam-Loaded Polymeric Micelle-like Nanoparticles for Safe Drug Administration during Pregnancy. *J. Microencapsul.* **2018**. <https://doi.org/10.1080/02652048.2018.1447615>.
- (106) Parker, A. L.; Newman, C.; Briggs, S.; Seymour, L.; Sheridan, P. J. Nonviral Gene Delivery: Techniques and Implications for Molecular Medicine. *Expert Reviews in Molecular Medicine*. 2003. <https://doi.org/10.1017/S1462399403006562>.
- (107) Levin, N.; Hendler-neumark, A.; Kamber, D.; Bisker, G. Enhanced Cellular Internalization of Near-Infrared Fluorescent Single-Walled Carbon Nanotubes Facilitated by a Transfection Reagent. *J. Colloid Interface Sci.* **2024**, *664* (March), 650–666. <https://doi.org/10.1016/j.jcis.2024.03.039>.
- (108) Hayashida, T.; Umemura, K. Atomic Force Microscopy of DNA-Wrapped Single-Walled Carbon Nanotubes in Aqueous Solution. *Colloids Surfaces B Biointerfaces* **2016**. <https://doi.org/10.1016/j.colsurfb.2016.03.068>.
- (109) Zheng, M.; Jagota, A.; Strano, M. S.; Santos, A. P.; Barone, P.; Chou, S. G.; Diner, B. A.; Dresselhaus, M. S.; McLean, R. S.; Onoa, G. B.; Samsonidze, G. G.; Semke, E. D.; Usrey, M.; Watts, D. J. Structure-Based Carbon Nanotube Sorting by Sequence-Dependent DNA Assembly. *Science* (80-.). **2003**. <https://doi.org/10.1126/science.1091911>.
- (110) Pensado, A.; Seijo, B.; Sanchez, A. Current Strategies for DNA Therapy Based on Lipid Nanocarriers. *Expert Opinion on Drug Delivery*. 2014. <https://doi.org/10.1517/17425247.2014.935337>.
- (111) Sinclair, F.; Begum, A. A.; Dai, C. C.; Toth, I.; Moyle, P. M. Recent Advances in the Delivery and Applications of Nonviral CRISPR/Cas9 Gene Editing. *Drug Deliv. Transl. Res.* **2023**, *9*, 1500–1519. <https://doi.org/10.1007/s13346-023-01320-z>.
- (112) Ali, H. S.; Boshra, M. S.; El Meteini, M. S.; Shafei, A. E. S.; Matboli, M. LncRNA-

- RP11-156p1.3, Novel Diagnostic and Therapeutic Targeting via CRISPR/Cas9 Editing in Hepatocellular Carcinoma. *Genomics* **2020**. <https://doi.org/10.1016/j.ygeno.2020.06.020>.
- (113) Seidl, C. I.; Fulga, T. A.; Murphy, C. L. CRISPR-Cas9 Targeting of MMP13 in Human Chondrocytes Leads to Significantly Reduced Levels of the Metalloproteinase and Enhanced Type II Collagen Accumulation. *Osteoarthr. Cartil.* **2019**, *27* (1), 140–147. <https://doi.org/10.1016/j.joca.2018.09.001>.
- (114) Naumov, A. V.; Ghosh, S.; Tsyboulski, D. A.; Bachilo, S. M.; Weisman, R. B. Analyzing Absorption Backgrounds in Single-Walled Carbon Nanotube Spectra. *ACS Nano* **2011**. <https://doi.org/10.1021/nn1035922>.
- (115) Zheng, Y.; Sanchez, S. R.; Bachilo, S. M.; Weisman, R. B. Indexing the Quality of Single-Wall Carbon Nanotube Dispersions Using Absorption Spectra. *J. Phys. Chem. C* **2018**. <https://doi.org/10.1021/acs.jpcc.7b12441>.
- (116) Zhou, J. N.; Rautio, T. C.; Liu, C.; Xu, X. Y.; Wang, D. Q.; Guo, Y.; Eriksson, J.; Zhang, H. Delivery of Protein Kinase a by CRISPRMAX and Its Effects on Breast Cancer Stem-like Properties. *Pharmaceutics* **2021**. <https://doi.org/10.3390/pharmaceutics13010011>.
- (117) Chittasupho, C.; Lirdprapamongkol, K.; Kewsuwan, P.; Sarisuta, N. Targeted Delivery of Doxorubicin to A549 Lung Cancer Cells by CXCR4 Antagonist Conjugated PLGA Nanoparticles. *Eur. J. Pharm. Biopharm.* **2014**, *88* (2), 529–538. <https://doi.org/10.1016/j.ejpb.2014.06.020>.
- (118) Pan, A.; Jakaria, M. G.; Meenach, S. A.; Bothun, G. D. Radiofrequency and Near-Infrared Responsive Core-Shell Nanostructures Using Layersome Templates for Cancer Treatment. *ACS Appl. Bio Mater.* **2020**. <https://doi.org/10.1021/acsabm.9b00797>.
- (119) Kuen, C. Y.; Galen, T.; Fakurazi, S.; Othman, S. S.; Masarudin, M. J. Increased

- Cytotoxic Efficacy of Protocatechuic Acid in A549 Human Lung Cancer Delivered via Hydrophobically Modified-Chitosan Nanoparticles as an Anticancer Modality. *Polymers (Basel)*. **2020**. <https://doi.org/10.3390/POLYM12091951>.
- (120) Saravanakumar, K.; Hu, X.; Shanmugam, S.; Chelliah, R.; Sekar, P.; Oh, D. H.; Vijayakumar, S.; Kathiresan, K.; Wang, M. H. Enhanced Cancer Therapy with PH-Dependent and Aptamer Functionalized Doxorubicin Loaded Polymeric (Poly D, L-Lactic-Co-Glycolic Acid) Nanoparticles. *Arch. Biochem. Biophys.* **2019**. <https://doi.org/10.1016/j.abb.2019.07.004>.
- (121) Mogheri, F.; Jokar, E.; Afshin, R.; Akbari, A. A.; Dadashpour, M.; Firouzi-amandi, A.; Serati-Nouri, H.; Zarghami, N. Co-Delivery of Metformin and Silibinin in Dual-Drug Loaded Nanoparticles Synergistically Improves Chemotherapy in Human Non-Small Cell Lung Cancer A549 Cells. *J. Drug Deliv. Sci. Technol.* **2021**. <https://doi.org/10.1016/j.jddst.2021.102752>.
- (122) Akbari, E.; Mousazadeh, H.; Hanifehpour, Y.; Mostafavi, E.; Gorabi, A. M.; Nejati, K.; keyhanvar, P.; Pazoki-Toroudi, H.; Mohammadhosseini, M.; Akbarzadeh, A. Co-Loading of Cisplatin and Methotrexate in Nanoparticle-Based PCL-PEG System Enhances Lung Cancer Chemotherapy Effects. *J. Clust. Sci.* **2022**. <https://doi.org/10.1007/s10876-021-02101-9>.
- (123) Kuhn, D. A.; Vanhecke, D.; Michen, B.; Blank, F.; Gehr, P.; Petri-Fink, A.; Rothen-Rutishauser, B. Different Endocytotic Uptake Mechanisms for Nanoparticles in Epithelial Cells and Macrophages. *Beilstein J. Nanotechnol.* **2014**. <https://doi.org/10.3762/bjnano.5.174>.
- (124) Tan, E.; Chin, C. S. H.; Lim, Z. F. S.; Ng, S. K. HEK293 Cell Line as a Platform to Produce Recombinant Proteins and Viral Vectors. *Frontiers in Bioengineering and Biotechnology*. 2021. <https://doi.org/10.3389/fbioe.2021.796991>.
- (125) Abaandou, L.; Quan, D.; Shiloach, J. Affecting Hek293 Cell Growth and

- Production Performance by Modifying the Expression of Specific Genes. *Cells* **2021**. <https://doi.org/10.3390/cells10071667>.
- (126) Subedi, G. P.; Johnson, R. W.; Moniz, H. A.; Moremen, K. W.; Barb, A. High Yield Expression of Recombinant Human Proteins with the Transient Transfection of HEK293 Cells in Suspension. *J. Vis. Exp.* **2015**. <https://doi.org/10.3791/53568>.
- (127) Chin, C. L.; Goh, J. B.; Srinivasan, H.; Liu, K. I.; Gowher, A.; Shanmugam, R.; Lim, H. L.; Choo, M.; Tang, W. Q.; Tan, A. H. M.; Nguyen-Khuong, T.; Tan, M. H.; Ng, S. K. A Human Expression System Based on HEK293 for the Stable Production of Recombinant Erythropoietin. *Sci. Rep.* **2019**. <https://doi.org/10.1038/s41598-019-53391-z>.
- (128) Kimura, T.; Ferran, B.; Tsukahara, Y.; Shang, Q.; Desai, S.; Fedoce, A.; Pimentel, D. R.; Luptak, I.; Adachi, T.; Ido, Y.; Matsui, R.; Bachschmid, M. M. Production of Adeno-Associated Virus Vectors for in Vitro and in Vivo Applications. *Sci. Rep.* **2019**. <https://doi.org/10.1038/s41598-019-49624-w>.
- (129) Bulcha, J. T.; Wang, Y.; Ma, H.; Tai, P. W. L.; Gao, G. Viral Vector Platforms within the Gene Therapy Landscape. *Signal Transduction and Targeted Therapy*. **2021**. <https://doi.org/10.1038/s41392-021-00487-6>.
- (130) Lin, P.; Shen, G.; Guo, K.; Qin, S.; Pu, Q.; Wang, Z.; Gao, P.; Xia, Z.; Khan, N.; Jiang, J.; Xia, Q.; Wu, M. Type III CRISPR-Based RNA Editing for Programmable Control of SARS-CoV-2 and Human Coronaviruses. *Nucleic Acids Res.* **2022**. <https://doi.org/10.1093/nar/gkac016>.
- (131) Qiao, J.; Sun, W.; Lin, S.; Jin, R.; Ma, L.; Liu, Y. Cytosolic Delivery of CRISPR/Cas9 Ribonucleoproteins for Genome Editing Using Chitosan-Coated Red Fluorescent Protein. *Chem. Commun.* **2019**. <https://doi.org/10.1039/c9cc00010k>.
- (132) Safaee, M. M.; Gravely, M.; Lamothe, A.; McSweeney, M.; Roxbury, D.

- Enhancing the Thermal Stability of Carbon Nanomaterials with DNA. *Sci. Rep.* **2019**. <https://doi.org/10.1038/s41598-019-48449-x>.
- (133) Heller, D. A.; Baik, S.; Eurell, T. E.; Strano, M. S. Single-Walled Carbon Nanotube Spectroscopy in Live Cells: Towards Long-Term Labels and Optical Sensors. *Adv. Mater.* **2005**, *17* (23), 2793–2799. <https://doi.org/10.1002/adma.200500477>.
- (134) Sipos, A.; Kim, K. J.; Sioutas, C.; Crandall, E. D. Evidence for Nanoparticle-Induced Lysosomal Dysfunction in Lung Adenocarcinoma (A549) Cells. *Int. J. Mol. Sci.* **2019**. <https://doi.org/10.3390/ijms20215253>.
- (135) Perevedentseva, E.; Hong, S. F.; Huang, K. J.; Chiang, I. T.; Lee, C. Y.; Tseng, Y. T.; Cheng, C. L. Nanodiamond Internalization in Cells and the Cell Uptake Mechanism. *J. Nanoparticle Res.* **2013**. <https://doi.org/10.1007/s11051-013-1834-8>.
- (136) Sahay, G.; Kim, J. O.; Kabanov, A. V.; Bronich, T. K. The Exploitation of Differential Endocytic Pathways in Normal and Tumor Cells in the Selective Targeting of Nanoparticulate Chemotherapeutic Agents. *Biomaterials* **2010**. <https://doi.org/10.1016/j.biomaterials.2009.09.101>.
- (137) MANDERS, E. M. M.; VERBEEK, F. J.; ATEN, J. A. Measurement of Colocalization of Objects in Dual-colour Confocal Images. *J. Microsc.* **1993**. <https://doi.org/10.1111/j.1365-2818.1993.tb03313.x>.
- (138) Dunn, K. W.; Kamocka, M. M.; McDonald, J. H. A Practical Guide to Evaluating Colocalization in Biological Microscopy. *American Journal of Physiology - Cell Physiology.* 2011. <https://doi.org/10.1152/ajpcell.00462.2010>.
- (139) Bolte, S.; Cordelières, F. P. A Guided Tour into Subcellular Colocalization Analysis in Light Microscopy. *Journal of Microscopy.* 2006. <https://doi.org/10.1111/j.1365-2818.2006.01706.x>.
- (140) Susin, S. A.; Daugas, E.; Ravagnan, L.; Samejima, K.; Zamzami, N.; Loeffler, M.;

- Costantini, P.; Ferri, K. F.; Irinopoulou, T.; Prévost, M. C.; Brothers, G.; Mak, T. W.; Penninger, J.; Earnshaw, W. C.; Kroemer, G. Two Distinct Pathways Leading to Nuclear Apoptosis. *J. Exp. Med.* **2000**. <https://doi.org/10.1084/jem.192.4.571>.
- (141) Ormerod, M. G.; Sun, X. M.; Brown, D.; Snowden, R. T.; Cohen, G. M. Quantification of Apoptosis and Necrosis by Flow Cytometry. *Acta Oncol. (Madr)*. **1993**. <https://doi.org/10.3109/02841869309093620>.
- (142) Cao, H.; Li, C.; Qi, W.; Meng, X.; Tian, R.; Qi, Y.; Yang, W.; Li, J. Synthesis, Cytotoxicity and Antitumour Mechanism Investigations of Polyoxometalate Doped Silica Nanospheres on Breast Cancer MCF-7 Cells. *PLoS One* **2017**. <https://doi.org/10.1371/journal.pone.0181018>.
- (143) Jiang, T.; Amadei, C. A.; Gou, N.; Lin, Y.; Lan, J.; Vecitis, C. D.; Gu, A. Z. Toxicity of Single-Walled Carbon Nanotubes (SWCNTs): Effect of Lengths, Functional Groups and Electronic Structures Revealed by a Quantitative Toxicogenomics Assay. *Environ. Sci. Nano* **2020**. <https://doi.org/10.1039/d0en00230e>.
- (144) Zhang, Y.; Xu, Y.; Li, Z.; Chen, T.; Lantz, S. M.; Howard, P. C.; Paule, M. G.; Slikker, W.; Watanabe, F.; Mustafa, T.; Biris, A. S.; Ali, S. F. Mechanistic Toxicity Evaluation of Uncoated and PEGylated Single-Walled Carbon Nanotubes in Neuronal PC12 Cells. *ACS Nano* **2011**. <https://doi.org/10.1021/nn2016259>.
- (145) Blanco, E.; Shen, H.; Ferrari, M. Principles of Nanoparticle Design for Overcoming Biological Barriers to Drug Delivery. *Nature Biotechnology*. **2015**. <https://doi.org/10.1038/nbt.3330>.

Appendix

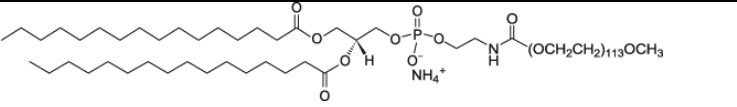
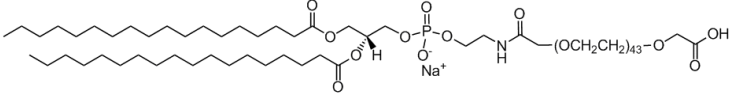
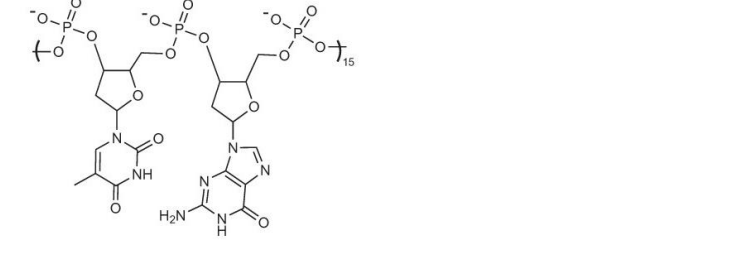
<p>16:0 PEG5000 PE *DPPE-PEG</p>	
<p>DSPE-PEG(2000) Carboxylic Acid *DSPE-PEG</p>	
<p>(GT)₁₅</p>	

Table A1. PEGylated lipids and ssDNA used in this research for suspending SWCNTs. The number adjacent to PEG is its molecular weight in Daltons. The chemical structure of (GT)₁₅ was reproduced with permission from Springer Nature⁵⁹.

* The name of the molecule used throughout the manuscript.

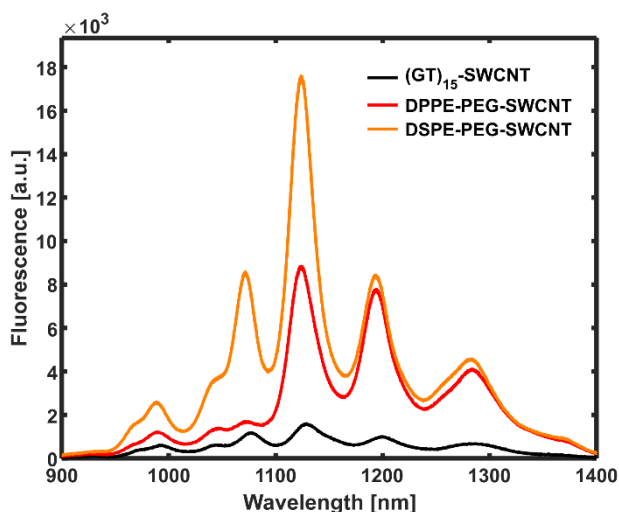


Figure A1. Fluorescence spectra of 1 mg L^{-1} of the various SWCNTs samples, excited by a 730 nm laser. The fluorescence intensity of both the PEG-SWCNT suspensions is noticeably higher than the $(\text{GT})_{15}$ -SWCNT fluorescence, while for most chiralities, the fluorescence of DSPE-PEG-SWCNTs is higher than the fluorescence of DPPE-PEG-SWCNTs.

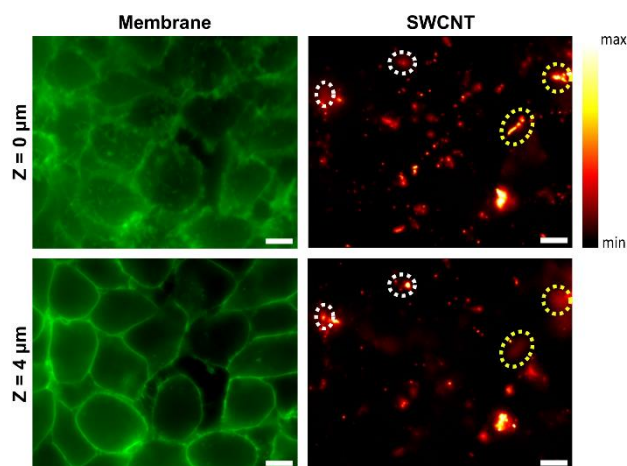


Figure A2. Images of HEK293T cells following overnight incubation with 0.3 mg L^{-1} $(\text{GT})_{15}$ -SWCNTs for different Z positions. The images were obtained using a $100\times$ objective. Scale bars for all images are $10 \mu\text{m}$. Top row: $Z = 0 \mu\text{m}$, the bottom surface of the cell, and bottom row: $Z = 4 \mu\text{m}$ inner surface of the cell. Left column: the cell membranes, stained with Cell Mask, imaged in the visible fluorescence channel, and right column: the SWCNTs imaged in the NIR fluorescence channel. The yellow dashed ellipses mark SWCNTs that are in focus in the $Z = 0 \mu\text{m}$ surface, where the membrane appears out of focus, and are out of focus in $Z = 4 \mu\text{m}$ surface, indicating that these SWCNTs adhered to the exterior surface of the cells. The white dashed ellipses mark SWCNTs that appear in focus in the $Z = 4 \mu\text{m}$ surface, where the membrane appears in focus as well, and are out of focus in the $Z = 0 \mu\text{m}$ surface, indicating that these SWCNTs were internalized by the cells.

תקציר

ננו-חלקיקים עם ממדים בסדר גודל דומה לממדים של אברונים תוך תאיים מהווים בסיס לטכנולוגיה מבטיחה עבור יישומים ביו-רפואיים ברמה התאית, הכוללים חישה ביולוגית, הדמיה וכלי למתן תרופות. ישנה חשיבות רבה לאופן כניסת הננו-חלקיקים לתאים הכוללת מעבר דרך ממברנת התא שמהווה מחסום לתא. המסלול העיקרי למעבר ננו-חלקיקים דרך ממברנת התא הוא אופנים שונים של אנדוציטוזה. בשנים האחרונות פותחו שיטות ננו-טכנולוגיות לשיפור החדירה דרך ממברנת התא. סוג אחד של ננו-חלקיקים בשם ננו-צינורות פחמן חד שכבתיות (Single-walled carbon nanotubes, SWCNTs) טומן בחובו פוטנציאל גדול ליישומים ביו-רפואיים מגוונים בשל התאימות הביולוגית לאחר איקטוב, ותכונות אופטיות, הכוללות קרינה פלורסנטית בטווח האינפרא-אדום הקרוב החופף לחלון השקיפות הביולוגית. באופן ספציפי, SWCNTs שימשו לכלי למתן תרופות לתאי מטרה, או לריפוי גנטי וכן כחיישנים לסמנים ביולוגיים תוך-תאיים שונים. בדומה לננו-חלקיקים אחרים, הדרך העיקרית של חדירת SWCNTs לתוך תאים היא אנדוציטוזה, לכן ישנה חשיבות ליעול שיטת ההכנסה התוך תאית של ה-SWCNTs. במחקר זה, אנו מציעים גישה חדשנית, המיעדת מחדש ריאגנט טרנספקציה לשיפור תהליך הכנסת SWCNTs לתאים. אנו חוקרים סוגים שונים של אקטוב של SWCNTs, ביניהם DNA חד-גדילי (ssDNA) או ליפידים PEGylated, ושני סוגי תאים שונים, תאי כליה עובריים ותאים אדנוקרצינומים מרקמת ריאה. אנו מראים שהכנסת PEGylated SWCNTs לתאים יעילה יותר בנוכחות ריאגנט הטרנספקציה, כאשר היעילות של הכנסת PEGylated SWCNTs בעל מטען שלילי בנוכחות ריאגנט הטרנספקציה בולטת יותר. לעומת זאת, ssDNA-SWCNTs נוטים ליצור צברים בנוכחות ריאגנט הטרנספקציה, כך ששיטה זו ליעול החדרת SWCNTs לתאים אינה מתאימה עבורם. בכל המקרים, כימות ה-SWCNTs שחדרו לתאים נעשה ע"י דימות במיקרוסקופ פלואורסצנטי בטווח האינפרא-אדום, המראה כי ה-SWCNTs לרוב ממוקמים בתוך הליזוזומים. באופן כללי, ההכנסה תוך תאית של ה-SWCNTs הייתה גבוהה יותר בתאים האדנוקרצינומיים, ובכך מעודדת יצירת שיטות חדשות לאספקת תרופות וחישה בתאים ממאירים.

אוניברסיטת תל - אביב

הפקולטה להנדסה ע"ש איבי ואלדר פליישמן

בית הספר לתארים מתקדמים ע"ש זנדמן-סליינר

שיפור חזירת ננו צינורות הפחמן חד שכבתיות לתוך תאים

ביולוגים חיים על ידי שימוש בריאגנט טרנספקציה וכימותה

באמצעות הדמיה פלורסנטית באינפורה אדום

חיבור זה הוגש כעבודת גמר לקראת התואר "מוסמך אוניברסיטה" בהנדסה ביו-רפואית

על-ידי

נעמה לויין

העבודה נעשתה במחלקה להנדסה ביו-רפואית

בהנחיית פרופ' גילי ביסקר

טבת התשפ"ד

אוניברסיטת תל - אביב

הפקולטה להנדסה ע"ש איבי ואלדר פליישמן

בית הספר לתארים מתקדמים ע"ש זנדמן-סליינר

שיפור חזירת ננו צינורות פחמן חד שכבתיות לתוך תאים ביולוגים חיים על ידי שימוש בריאגנט טרנספקציה וכימותה באמצעות הדמיה פלורסנטית באינפורה אדום

חיבור זה הוגש כעבודת גמר לקראת התואר "מוסמך אוניברסיטה" בהנדסה ביו-רפואית

על-ידי

נעמה לויך

טבת התשפ"ד